

STUDY OF FLOW INTERACTION BETWEEN MULTIPLE
STAGES IN LONG HORIZONTAL WELLS

A Dissertation

Presented to

the Faculty of the Department of Mechanical Engineering

University of Houston

In Partial Fulfillment

of the Requirements for the Degree

Doctor of Philosophy

in Mechanical Engineering

by

Pranab Narayan Jha

December 2014

STUDY OF FLOW INTERACTION BETWEEN MULTIPLE STAGES IN LONG HORIZONTAL WELLS

Pranab Narayan Jha

Approved:

Chair of the Committee
Ralph W. Metcalfe, Professor,
Mechanical Engineering

Committee Members:

Dong Liu, Associate Professor,
Mechanical Engineering

Bonnie Dunbar, Professor,
Mechanical Engineering

Stanley Kleis, Professor Emeritus,
Mechanical Engineering

Giles Auchmuty, Professor,
Mathematics

Suresh K. Khator
Associate Dean,
Cullen College of Engineering

Pradeep Sharma
M.D. Anderson Chair Professor &
Department Chair,
Mechanical Engineering

Acknowledgments

First, I would like to express my deepest gratitude to my advisor, Prof. Ralph W. Metcalfe, for his guidance and patience with me for the last five years. I am thankful for the opportunity to work with him on some very interesting problems. He has been a constant source of advice and motivation.

I would like to thank the University of Houston's Research Computing Center and the Center for Advanced Computing and Data Systems (CACDS) for the computational resources. This work was partly funded by Apache Corporation. I would like to mention Chuck Smith (Apache) for his inputs on the wellbore flow problem and lucidly conveying ideas from an industry viewpoint. I also thank Prof. Stan Kleis for teaching me the fundamentals of turbulence course and his guidance on the Blowout Preventer project.

I would like to acknowledge my colleagues - Haripriya Sundararaju, Ethan Pedneau, Hilario Torres ¹, Aishwarya Mantha, ² and Mircea Ionescu ³ - for providing support and a friendly environment to work in. Trina Johnson deserves a special mention for her help throughout my graduate studies. Many other individuals who have not been named here but have been a part of my work-life or otherwise, making me feel at home away from home, deserve my gratitude.

My work would not have been possible without the support of my beautiful wife, Payal, who was very patient with me throughout. Finally, I dedicate this dissertation to my parents, whose faith and blessings have fueled this journey.

¹currently at Stanford University

²currently at Fluor Corporation

³currently at Cameron International

STUDY OF FLOW INTERACTION BETWEEN MULTIPLE
STAGES IN LONG HORIZONTAL WELLS

An Abstract

of a

Dissertation

Presented to

the Faculty of the Department of Mechanical Engineering

University of Houston

In Partial Fulfillment

of the Requirements for the Degree

Doctor of Philosophy

in Mechanical Engineering

by

Pranab Narayan Jha

December 2014

Abstract

Numerical simulation of flow inside a horizontal wellbore with multiple completion stages is presented. The aim was to study the blocking effect on the toe-end stages observed in long horizontal wells. An axisymmetric pipe geometry was used to model the wellbore, with circumferential inlets representing perforation stages. Firstly, using a simplified five-stage case with steady state flow conditions, the existence of three basic flow regimes - trickle flow, partially blocked flow and fully blocked flow - was established. Using these results, the phenomenon of blocking of upstream inlets near the toe by the downstream ones near the heel is explained. The existence of these flow regimes is consistent with well-log data obtained from a horizontal shale gas well with 31 completion stages at two different times during production.

To study the dynamic behavior of the completion stages when reservoir fluid flows into the wellbore, a basic reservoir depletion model was created using a pressure boundary condition at the circumferential inlets, varying in time. A lumped-parameter model was used to account for the pressure drop between two inlets separated by large axial distance. Different characteristic time scales, related to the depletion of the reservoirs, were identified. By varying initial conditions, the dynamic behavior of the system with multiple inlets was observed and analyzed. The transition of flow regimes with depletion of reservoirs is consistent with the observed behavior of the horizontal shale gas well.

A simple nozzle design was used to modify the entry of flow from the inlets into the wellbore. The interaction between wellbore stages in presence of nozzles is studied using a two-dimensional mesh with the reservoir depletion and inter-stage pressure drop model. The nozzle opening size was varied to achieve production enhancement over simulated time period. This provides an alternate method of inflow control that could be used to homogenize production from different well stages. This would make

use of the already perforated pipe wall without having to use a screen around the production pipe.

In addition, three-dimensional geometry of a combustor was used to simulate flow from discrete perforations into the pipe crossflow. An initial analysis of flow through the nozzle design on a single inlet was conducted using a three-dimensional mesh. Mean flow analysis of these simulations and comparison of pressure drop between the nozzle and combustor cases is presented.

Table of Contents

Acknowledgments	iv
Abstract	vi
Table of Contents	viii
List of Figures	x
List of Tables	xiii
1. Introduction	1
1.1. Background	1
1.2. Objective	3
2. Literature Review	6
3. Computational Details	16
3.1. Geometry and Mesh	16
3.1.1. Two dimensional axisymmetric pipe domain with five crossflow inlets	16
3.1.2. Two dimensional axisymmetric pipe domain with nozzles at inlets	18
3.1.3. Three dimensional combustor geometry	20
3.1.4. Three dimensional nozzle geometry	21
3.2. Governing equations	22
3.2.1. Turbulence Modeling	23
3.2.2. $k - \epsilon$ model	24
3.3. One dimensional friction factor model	25

3.4. Numerical Method	25
4. Results and Discussion	27
4.1. Mesh resolution	27
4.2. System in steady state	29
4.2.1. Relative pressure drop	29
4.2.2. Modeling inter-zone distance	31
4.2.3. Effect of inlet size	33
4.3. Time dependent cases	34
4.3.1. Effect of inlet size	36
4.3.2. Smaller volume: Initial transients	42
4.3.3. Effect of Reservoir Volume	45
4.4. Nozzles on inlets	46
4.4.1. Steady state analysis - Flow regime	48
4.4.2. Time-dependence of flow regimes	51
4.5. Annular inlet with discrete holes	53
4.5.1. Code Validation	53
4.5.2. Mean flow	59
4.6. Annular jet pump - three-dimensional simulations	60
5. Conclusions	68
6. Future work	71
References	72
Appendix	79

List of Figures

1.1.	Horizontal drilling and hydraulic fracturing (Source: EPA)	1
1.2.	Cumulative production curves for a horizontal shale gas well at two different times from start of production, from well log data.	2
1.3.	Variation of Re and Ma along the wellbore at 30 and 155 days, from well log data.	3
2.1.	Schematic of a general setup of perforation flow mixing with cross flow	7
2.2.	Schematic of Combustor and Inflow Control Device.	12
2.3.	Main parts of an annular jet pump	13
3.1.	Schematic of 2D geometry with five crossflow inlets and relevant dimensions.	17
3.2.	Schematic of 2D axisymmetric configuration with nozzle geometry on an inlet for modifying flow entry.	19
3.3.	Schematic of 3D geometry of a pipe with a nozzle.	20
3.4.	Schematic of 3D domain with nozzle geometry installed on a single inlet.	22
4.1.	Comparison between three different mesh resolutions for 2D axisymmetric domain.	28
4.2.	Friction factor comparison for wellbore flow	31
4.3.	Comparing flow rate and pressure profile along the well length for different axial separation between inlets.	32
4.4.	Steady state flow rates compared for Cases 1, 2 and 3.	34
4.5.	Flow rate, normalized flow rate and flow-regime change over time for case 1 (Table 4.1)	37

4.6. Normalized static pressure and drained volume for case 1 (Table 4.1) . . .	38
4.7. Regime change of system over time for cases 2 and 3.	39
4.8. Total flow rate at the heel over time compared for cases 1, 2 and 3. . . .	40
4.9. Volume drained over time from inlet 1 and 5 compared for case 1, 2 and 3.	41
4.10. Total volume drained for systems with different inlet sizes.	42
4.11. Comparison of drainage from inlet 1 and 5 for cases 4, 5 and 6.	43
4.12. Fraction of initial volume drained from each inlet at t=80s for Case 1, 2 & 3 and at t=40s for Case 4, 5 & 6. Total drainage takes into account all individual volumes.	44
4.13. Total flow rate comparison for different initial volumes.	45
4.14. Velocity vectors overlayed on pressure contours near the jet pump nozzle for inlets 1 and 3 for <i>JP-eq1</i> case	47
4.15. Steady state flow regimes for jet pump cases	48
4.16. Comparison of jet pump cases with circumferential inlet cases	50
4.17. Flow regimes and volume drained over time for cases with annular jet pump inlets.	52
4.18. Volume drained for three cases with nozzles on inlets at t=80s.	53
4.19. Comparison of axial velocity for combustor geometry crossflow at different axial locations.	54
4.20. Comparison of friction factor across the jet with experimental data . . .	56
4.21. Comparison of jet trajectories for two different velocity ratios with pub- lished data	57
4.22. Comparison of jet trajectories for two different values of scalar diffusivity.	58
4.23. Comparison of jet trajectories for different velocity ratios.	59
4.24. Comparison of axial velocity for combustor geometry crossflow at different axial locations.	61
4.25. Contours of various quantities of the flow in the mixing region	62

4.26. Axial velocity profile comparison for mesh resolution test of 3D simulation	63
4.27. Pressure and x-velocity contours on center plane for 3D simulation of inlet with nozzle.	64
4.28. Axial velocity profiles downstream of the jet injection plane. $Re_{cf} = 5700$.	65
4.29. Friction factor comparison between discrete holes and nozzle	66
A.1. Comparison of turbulence models and development length	80
A.2. Friction factor comparison and velocity contours from simulations	82

List of Tables

1.1. Gas properties for computing Ma	4
4.1. Transient simulation cases using 2D axisymmetric geometry.	30
4.2. Simulation cases with nozzles at inlets	46

1. Introduction

1.1. Background

Hydraulic fracturing is a common practice in completion and production of oil and natural gas from hydrocarbon reservoirs, mainly consisting of shale rock formations. When used in conjunction with horizontal drilling for production of natural gas or oil, it enables extraction of hydrocarbons from reservoirs with low permeability (in nano Darcy) which is difficult to produce otherwise. This involves injection of water, sand and chemicals under high pressure into the rock formation containing hydrocarbons, using the drilled well. This increases the size of existing fractures in the rocks and creates new ones for oil or gas to enter the well due to pressure gradient.

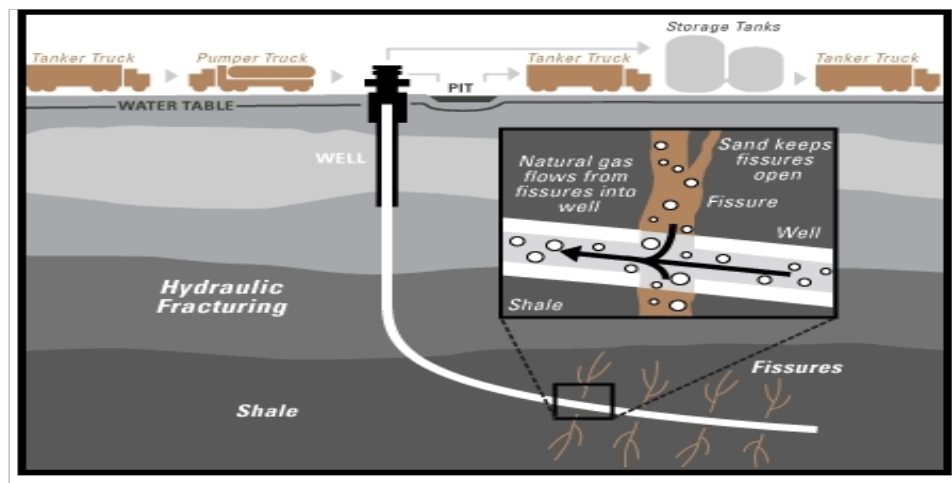


Figure 1.1: Horizontal drilling and hydraulic fracturing (Source: EPA)

Figure 1.1 shows the basic layout of these wells and the fracture system. The horizontal section of the well can have hundreds of feet between each fracture zone (known as a *stage*). The fractured zone includes a set of perforations through which water with chemicals and sand can be injected into the reservoir to create a path for the hydrocarbons to enter the well. American-Petroleum-Institute (2014) and King (2012) give an overview of the process and industry in general.

The pressure drop in the wellbore for various flow rates and fluid types, including multiphase systems, is potentially of great interest to the scientific community. The initial production after completing the fracturing process generates high flow rates. This high level of production usually exists only for a short time interval (on the order of few days) after which the system may evolve into a different flow regime depending on factors like the well length, number of stages, pressure draw-down, etc.

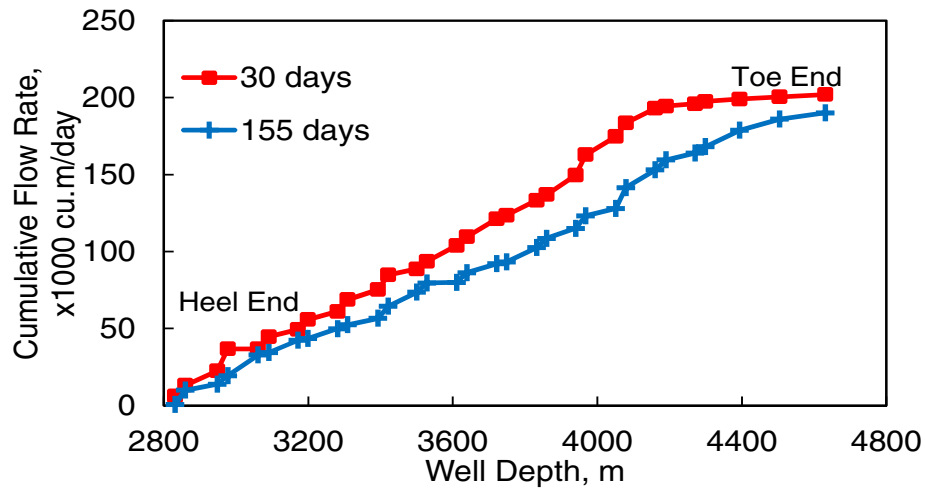


Figure 1.2: Cumulative production curves for a horizontal shale gas well at two different times from start of production, from well log data.

Figure 1.2 shows cumulative flow rate, starting with the first stage near the heel, for a horizontal natural gas well at two different time intervals from start of production. The points on the curves indicate the gas production at well logging sites along the wellbore against well length that spans about 1800 meters. From the first log (red curve) taken 30 days after beginning of production, it is observed that five or six stages near the toe end do not contribute substantially to the total production - a near-zero slope. The blue curve in the same figure, representing a log taken 155 days after start of production, shows lower cumulative production but the stages towards the toe-end are now producing. A similar behavior has been observed in liquid producing wells. Moreover, the density and viscosity of the gas phase at high pressure

and temperature is much different than at standard temperature and pressure (STP) conditions.

The energy industry estimates that less than 20% of the reserves in a reservoir are extracted using primary recovery technology that depends mainly on natural pressure of the reservoir (Zitha et al. (2008), Hiller (2014), DOE/EIA (2014)). The decrease in pressure below a certain threshold renders production from a well unfeasible without a pressure boosting mechanism such as gas lift which is still considered a part of primary recovery. The scope for improvement in total recovery has lead to innovation in the way drilling is done and wells are designed or *completed* for production. Enhanced Oil Recovery (EOR) techniques have been developed to get the maximum output possible from horizontal wells. Managing the reservoir pressure is an important aspect of the entire process and equipment like Inflow Control Devices (ICD) are increasingly being employed.

1.2. Objective

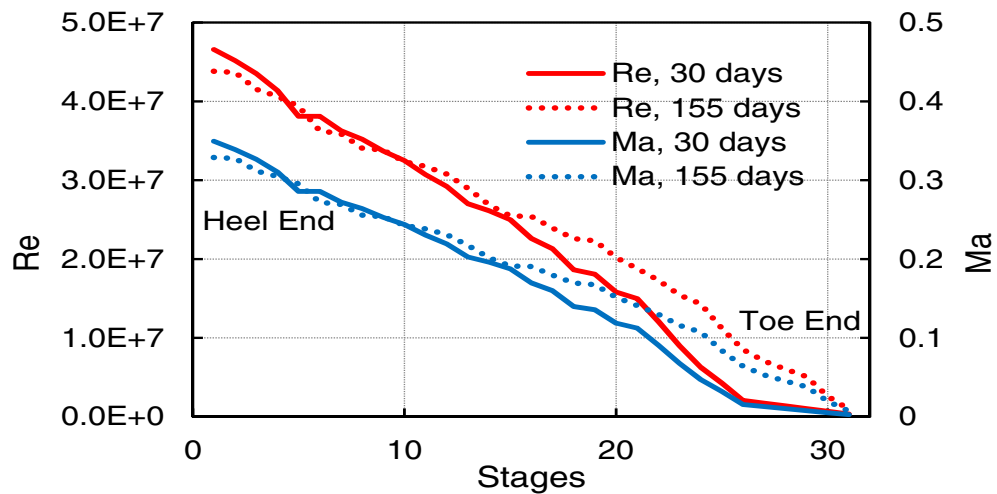


Figure 1.3: Variation of Re and Ma along the wellbore at 30 and 155 days, from well log data.

Figure 1.3 presents the well data set in terms of the relevant non-dimensional numbers. It shows the change in Reynolds number ($Re = \rho UD/\mu$) and Mach number

($Ma = v/c$) along the well length. With inflow from the perforation stages, the flow rate increased from the toe towards the heel resulting in increase of Re and Ma at corresponding locations. Here, ρ is fluid density, U is average velocity, D is pipe diameter, μ is fluid viscosity and c is speed of sound in the fluid. Table 1.1 lists the approximated fluid properties used for computing Re and Ma . High Re along the wellbore suggests that flow is turbulent at both logged instances along the wellbore. It can be observed from the 30-day curves that the Ma remained below 0.3 for a large fraction of the wellbore length, except for six stages near the heel. As the reservoir pressure decreased over time, flow rates also decreased. The 155-day curve suggests increase in Re and Ma towards the toe, but decrease near the heel. In a small section of the wellbore near the heel compressible effects may start to become important ($Ma > 0.3$). However, an incompressible flow model may be used to analyze the described behavior in remainder of the wellbore.

Table 1.1: Gas properties for computing Ma

P (kPa)	T (K)	ρ (kg/m ³)	μ (Pa-s)	D (m)	c (m/s)
6300	408	30	1.5E-5	0.127	528

In general for most wells the stages near the heel produce significantly more than the toe-end stages. This ‘heel-toe’ effect is ubiquitous in wellbores and is independent of the reservoir properties. The main objective of this work is to study this effect and possibly model it.

As observed from Figure 1.3, the toe stages that were not producing initially at the 30-day mark had started producing at the 150-day mark. This implied a change in the state of the well. One key objective is to study this change in the system comprising of the wellbore and multiple inlet stages distributed over length of the wellbore. How does this change in the system affect the total production of fluids from a well? Can total production be improved by modifying the geometry of the flow inlets? A major portion of the presented work will deal with the above issue

using computational fluid dynamics as a tool to simulate flow from these stages into the wellbore.

The flow into the wellbore from perforations is very similar to jets issuing in a cross flow, which has been studied extensively in the past. But the distribution of these perforations adds to the complexity and can affect the inflow and mixing near a perforation stage. This is an interesting phenomenon that needs further analysis.

Chapter 2 provides an overview of the published literature pertaining to various aspects of the problem discussed above including a review of jets in a confined cross-flow and annular jet-pumps. The numerical methods used to model the problem, including the geometry, boundary conditions and solution procedure are detailed in Chapter 3. Chapter 4 presents the results and discussion of numerical simulations that were conducted. This includes flow in horizontal wellbores with inflow points and also explores the possibility of using a jet-pump type configuration near the inflow zones to increase production. The conclusions from this study are presented in Chapter 5 and possible future directions in Chapter 6.

2. Literature Review

Many publications can be found describing flow in porous media (reservoir), fracture zones, skin effects and other related issues. Reservoir modeling is a problem well documented in the literature. Ouyang et al. (1998), Furui et al. (2005), Penmatcha and Aziz (1999), Karimi-Fard and Durlofsky (2011) and several others have studied reservoir dynamics and its effect on production from the wellbore. Most of these studies deal with one-dimensional models for flow in the wellbore. On the other hand, there is a scarcity of open literature on wellbore hydraulics analyzing flow in long horizontal wells with multiple stages, especially using accurate numerical simulations. Following is a summary of the key studies in this area.

Some of the earliest studies on pressure losses in a wellbore were carried out by Dikken (1990) and Su and Gudmundsson (1998). Dikken (1990) presented an analytical method to relate flow rate in a wellbore to the draw-down pressure and concluded that total production leveled off as a function of well length. As a simplification, he assumed single-phase flow in which the whole horizontal section was open for production. Laminar flow was not considered in this study. But as discussed earlier (and in following chapters), laminar flow can exist in a majority of the wellbore, specifically at later stages of production.

Some studies have considered modeling the pressure drop across a perforation zone using experimental data. Figure 2.1 shows a general schematic of the setup used in most of such experiments. This is geometrically similar to perforated liners commonly used in horizontal wells. The effects of perforation flow rate, geometry, density, etc. were usually studied. Su and Gudmundsson (1998) conducted experiments to determine pressure drop resulting from inflow through a perforated pipe. The total pressure drop across the perforated section increased with Reynolds number. The total pressure drop was divided into wall friction, flow acceleration, pipe roughness

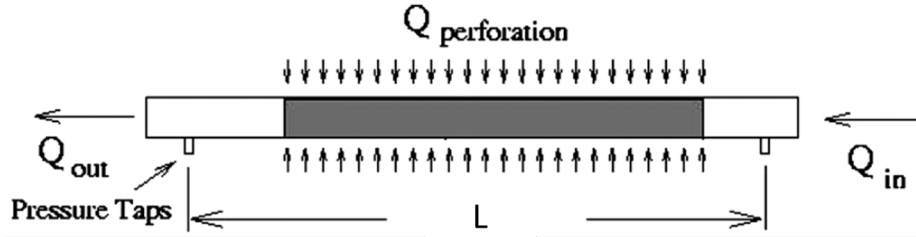


Figure 2.1: Schematic of a general setup of perforation flow mixing with cross flow, used in various studies in literature.

and fluid mixing contributions. They concluded that beyond a certain perforation-to-pipe flow rate limit the perforation inflow reduced the frictional pressure loss in a horizontal wellbore. This was attributed to lubrication effect by the perforation inflow and a modified pressure loss coefficient was used to model the pressure drop across the perforated section.

Similar experiments were carried out by Yuan et al. (1997) who investigated experimentally and theoretically, the frictional losses for flow across a single-perforation horizontal pipe, and made comparisons of their model with earlier published results of Asheim et al. (1992). Yalniz and Ozkan (2001) tried to relate the friction factor to a combination of Reynolds number, ratio of influx to wellbore flow rate and perforation to wellbore diameters. Jiang et al. (2001) studied experimentally the effect of completion geometry on liquid flow behavior in horizontal wells. They changed the perforation density and phasing and calculated the friction pressure losses for multiple cases. Generally, the friction factor is calculated as a function of the ratio of inflow to the main flow rate and the Reynolds number. Their experimental results provide a one-dimensional model to calculate pressure-drop for a given flow rate, geometry, etc. Some of these patterns will be used for comparison with numerical results presented in the current work. More recently, Zhang et al. (2014) have tried to come up with empirical and theoretical models for pressure profile in a horizontal well with inflow from perforation zones.

Ramamurthy and Zhu (1997) studied the pressure and energy losses in two di-

mensional flows past 90° junctions of rectangular closed conduits. They carried out experiments for different area ratios and made velocity and wall-pressure measurements. This experimental data set provided more details of the mixing process in the vicinity of the inflow, but used a simplified channel geometry. Also, only one inflow point was used, hence pressure drop between multiple zones cannot be established.

A computational study, that is relevant to the problem at hand, was performed by Vicente et al. (2002, 2004). They solved 1-D single-phase flow equations in the horizontal wellbore coupled with 3-D reservoir equations using a finite difference scheme. They considered radial influx of fluid into the wellbore at all discretized sections, and a constant mass flow rate at the outlet (heel). The 1-D nature of the flow equation did not give enough details of the wellbore flow. But the model showed that the flux along the wellbore length varied as a function of pressure and time. They compared their results with that from commercial code ECLIPSE. Similar results have been obtained using slightly different boundary conditions in the present study, that show the effect of a time-varying pressure at wellbore inflow points.

Hill and Zhu (2008) proposed analytic expressions that can be used to determine the relative effects of wellbore pressure drop and formation damage on horizontal well inflow, including skin effect. They showed that the wellbore pressure drop could be as high as 40% of the drawdown pressure under certain conditions like high-permeability in reservoirs. This might put an unwanted limitation on the productivity of wells in such reservoirs.

Experimental and numerical results of multiphase flow in horizontal pipes are widely available, both with and without radial inflow. Ouyang et al. (1998) presented a single phase flow model for wellbore flow completions in various configurations, including horizontal wells. Ouyang and Aziz (2000) addressed the problem of radial influx and outflux in a horizontal well by considering a homogeneous mixture model for gas-liquid flow. The pressure drop due to fluid expansion and due to wall

influx/outflux were considered in addition to the frictional and gravitational components in the calculation of the total pressure drop in the wellbore. There was, however, no effort made to relate the pressure at the inlet/outlet with the total outflow at the heel. Also, the time-dependence of wall-inlet pressure has not been looked at. In the present work, this aspect of inlet interaction has been studied.

The *heel-toe* effect is a common occurrence in horizontal wells in which the heel end produces at a higher flow rate than the toe end due to pressure losses associated with length of the pipe. Goswick and LaRue (2014) presented field data from experiments carried out on three wells using chemical tracers. The objective was to study contribution of individual stages of a horizontal well using a particular type of tracers. They found communication between some offset wells. Their results, both from oil and water soluble tracers, indicated the presence of significant heel-toe effect in these wells initially. The increased production from toe-end stages over time, with decrease in production from the heel-end stages was also evident.

Dore Fernandes et al. (2006) suggested a new improved oil recovery technology for obtaining equal production from all stages of a horizontal well. The objective was to homogenize the inflow profile along the well. This was achieved by increasing the density of perforations on the wellbore along the well length. The toe-end of the well had the maximum perforations and the heel-end had minimum.

Related research was found in other engineering applications that dealt with similar geometries and flow conditions to those in a horizontal wellbore. The design of storm water or sewer junctions in pressurized flows related to civil and hydraulic engineering has been studied extensively. Zhao et al. (2006) conducted experiments that categorized various flow regimes in sewer junctions with a steep outgoing pipe, based on the surcharge in the inlet and outlet pipes. They studied the variation of water depth in the junction chamber and presented results of energy losses and velocity measurements in surcharged flow. Marsalek (1984) studied experimentally the

head losses in a straight-flow-through junction with identical inflow and outflow pipe diameters. These flows are generally driven by gravity, rather than pressure, but have multiple entry points for flow merging into a main line which makes them similar to the current geometrical setup.

The presence of water and liquid hydrocarbons generates multiphase flow inside a horizontal natural gas well. Agrawal et al. (1973) performed experiments to calculate pressure drop and volume fraction data for horizontal stratified flow with air-oil two-phase mixtures. They also proposed a mechanistic model to calculate the pressure drop in two-phase flows. Taitel and Dukler (1976) analyzed the mechanisms for transition between different flow regimes. They developed a theoretical model that predicts the relationship between different flow variables. These relationships were used to develop a model for transition between the various flow regimes of two-phase flow in horizontal as well as inclined pipes. Multiphase flow is an important part of the production process with flow of solid, liquid and gas phases observed at different times. But in the present work the focus will be to study well behavior under single phase and isothermal conditions.

Kamotani and Greber (1972) studied the interaction among multiple jets aligned in a row entering normal to the cross-flow. Ali (2003) conducted experiments to study multiple jet interaction in a cross-flow in the absence of strong boundary effects. The experimental setup of Yu et al. (2006) also involved similar buoyant jets discharging into a perpendicular cross-flow. They found that the effective cross-flow that influenced the behavior of the downstream jets was significantly reduced due to the wake shadow as well as the entrainment demand in the momentum-dominated near-field of the leading edge jet. This was referred as the sheltering effect. Lai and Lee (2010) formulated a general semi-analytical model for multiple tandem jets in a cross-flow using a sink-doublet model for the jet entrainment to predict the sheltered velocity near the downstream jets. Such a setup resembles a wellbore flow with multiple

normal inflow points along a axial flow path.

The review paper by Mahesh (2013) provides a detailed description of the physical behavior and a survey of related literature on jets in a crossflow. Cambonie et al. (2013) conducted experiments in a water-tunnel using Particle Image Velocimetry (PIV). Their study focused on low velocity ratio (jet to cross-flow velocity) ranging from 0.5 to 3. They introduced a scaling law for the jet trajectory and a scaling quality factor to determine how well a given scaling collapses the trajectories.

Coletti et al. (2013) performed experimental work in a water tunnel investigating a turbulent jet, inclined at 30° issuing in a cross-flow. This setup is commonly found in film cooling applications, where mixing of the jet fluid with the crossflow fluid is very important. Magnetic Resonance Velocimetry, Magnetic Resonance Concentration measurements, and Particle Image Velocimetry were used for visualization of scalar and vector fields. They compared the jet entrainment with that of an axisymmetric jet with and without any crossflow. Jet entrainment was slightly enhanced compared with jet issuing in a quiescent fluid. Eddy viscosity was found to be very anisotropic and non-homogeneous. Numerical simulation of the configuration was also performed using the $k - \epsilon$ turbulence model available in Ansys-Fluent. The simulation predicted a higher eddy-viscosity leading to a lower strength of the Counter Rotating Vortex Pair (CRVP). Jet entrainment was also under-predicted by the turbulence model, downstream of the injection.

The geometric configuration in a wellbore stage consisting of multiple perforations also resembles closely a gas combustor. This geometry can be found in gas turbine burners and preburners in liquid rocket engines. Prière et al. (2005) conducted numerical and experimental investigation of a combustor design consisting of eight isothermal jets injecting into a round pipe. They performed Large Eddy Simulations of the flow using a single jet in a 45° section of the pipe and symmetry boundary conditions to account for the periodicity of the domain. The Reynolds

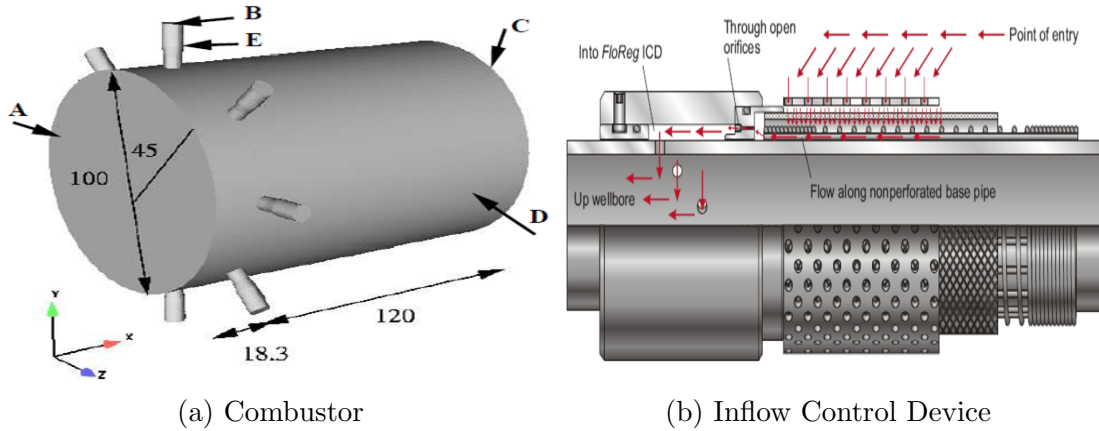


Figure 2.2: Schematic of Combustor and Inflow Control Device. (a) Combustor, source: Prière et al. (2005) (b) ICD, source: Aadnoy and Hareland (2009)

number of the flow in their work was about 1.68×10^5 and the flow was very close to being compressible. The speed of flow in oil wells is not close to the compressible limit but might well be for gas wells, as was discussed in the analysis of Fig. 1.3. A schematic of the domain used by Prière et al. (2005) is shown in Fig. 2.2a.

Davoudzadeh et al. (2012) also investigated simultaneous confined transverse jets issuing radially in an axisymmetric confined crossflow, geometrically similar to experiments of Prière et al. (2005). Their objective was to compare the performance of standard and realizable $k - \epsilon$ models using commercially available CFD software Ansys-Fluent, Star-CCM+ and CFD++. They used wall treatment options like standard, enhanced or low Re available in these codes. They compared velocity and scalar distribution with experimental data and concluded that standard $k - \epsilon$ using Fluent performed better than other models. This provides a basis of further investigation of flow through such geometry using two-equation models.

Controlling the flow from the inlets (jets) entering the pipe is very important. Recent field applications of Inflow Control Devices (ICD) have allowed engineers to design the wellbore such that unwanted gas or water does not have easy access into the well. Mathiesen et al. (2011), Halvorsen et al. (2013) and others have documented improvement in production from wells that have ICD installed on them. The appli-

cation of ICD helped in restricting the passage of flow into the wellbore near the heel due to an increased pressure drop. This allows more flow initially from the toe-end stages.

An example of the theory and design of an ICD can be obtained from published literature such as Fripp et al. (2013), Oyeka et al. (2014) and Birchenko et al. (2010). Figure 2.2b shows one variant of the many designs that are used in the industry. Aadnoy and Hareland (2009) give a detailed analysis of the flow and related pressure drop for their version of ICD.

Another way to control, and possibly enhance, production from the well can be by employing an annular jet pump configuration. In principle, this can be applied to entrain fluid using a high speed primary jet flow. The suitability of this application shall be explored in this thesis.

A jet pump is a device that is used to transfer momentum from a primary jet flow moving at a high velocity to a secondary flow. There are two basic types of jet pumps in use. The canonical center-type jet pump (CJP) has a high-speed flow in the center with low speed fluid entering from an annular opening. The annular jet pump (AJP), less commonly used, has an annular high-speed jet that entrains a secondary (suction) flow issuing at the center.

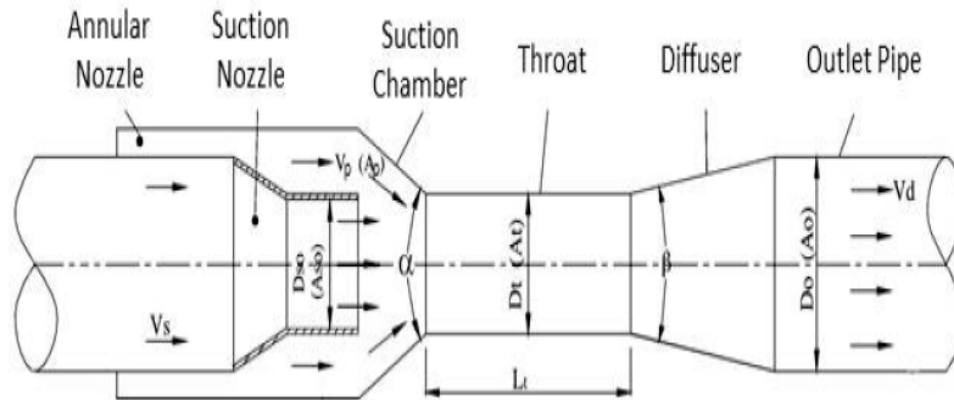


Figure 2.3: Main parts of an annular jet pump

Among the earliest experimental work on jet pumps was that carried out by

Gosline and O'Brien (1934). They looked at the efficiency of CJP with water as the working fluid. The main parts of an AJP are shown in Figure 2.3 (source: Shimizu et al. (1987)).

Winoto et al. (2000) presented a theoretical and experimental analysis of the efficiency of CJP. They studied the effect of area ratio of nozzle to mixing throat and different nozzle cross sections. They found the circular cross-section and area ratio of about 0.3 to be most efficient. The theoretical maximum efficiency of CJP is 100%, but that does not take the energy losses in various parts of the CJP into consideration. Shimizu et al. (1987) conducted experiments to study the performance of an AJP and its relation to the design. The maximum efficiency they obtained was 36%. Even with a minimal design modification to the pump - a straight mixing chamber entrance and area ratio of 0.27 - efficiency of upto 30% could be obtained. Our design consideration for the jet pump in the wellbore is based on a basic design from this work and the details will be presented in subsequent chapters. Elger et al. (1994) conducted an experimental investigation of the recirculation zone in the mixing chamber of an AJP. They presented a discussion of the design parameters and design space to avoid recirculation. Momentum ratio was identified as the key parameter for the onset (and avoidance) of recirculation. Long et al. (2012) carried out CFD simulation of incompressible steady flow in an AJP using different designs. They used a two-dimensional axisymmetric domain to simplify the geometry and computational costs. The turbulence modeling was done using a realizable $k - \epsilon$ model. They obtained a maximum efficiency of 35.8% and concluded that the flow ratio and mixing length had the most influence on the AJP.

Sadr and Klewicki (2003) presented results of an experimental study of coaxial jets. This configuration resembles closely that of a jet pump. The Reynolds number based on the core flow (suction) was $Re = 4.1 \times 10^4$. But the tested velocity ratios (outer to core velocity) ranged from $r_v = 0.18$ to 1.1. This made the outer flow as the

suction and inner flow as main jet. This assembly is closer to the CJP. They provided details of the flow field using molecular tagging velocimetry (MTV) method, including mean velocity, turbulence intensities and higher order moments. This makes the data set a very good source for comparison and testing of numerical codes.

As mentioned earlier, limited effort has been made to study wellbore flow of either single or multi-phase nature and such works are found wanting in accuracy. Ragab et al. (2008a,b) have simulated two-phase flow in a long horizontal pipe without radial influx, including intermittent flow regimes. They used a very coarse mesh with the volume of fluid (VOF) model proposed by Hirt and Nichols (1981). The mesh uses a very large aspect ratio which exceeds a reasonable value for accurate interface tracking.

The time-dependence of such flows in horizontal wells has not been explored. It is understood that with decrease in reservoir drawdown pressure, the inflow in the wellbore will also decrease which will change the productivity (ratio of production rate to drawdown pressure) along the well.

3. Computational Details

3.1. Geometry and Mesh

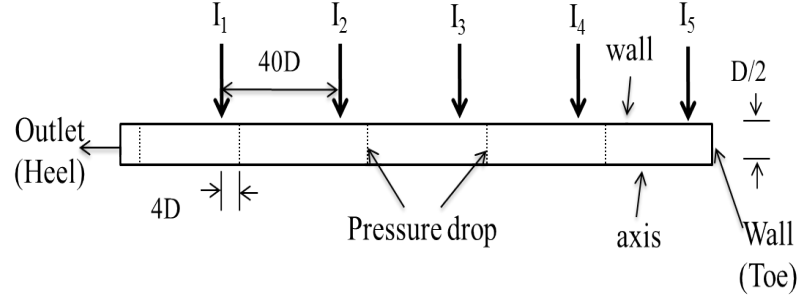
This section describes the various geometries and meshes used for the simulations. Both two-dimensional (2D) and three-dimensional (3D) geometries were used and details are presented here. The mesh was generated for each geometry using Ansys Meshing program and solution obtained using Ansys Fluent package.

3.1.1. Two dimensional axisymmetric pipe domain with five crossflow inlets

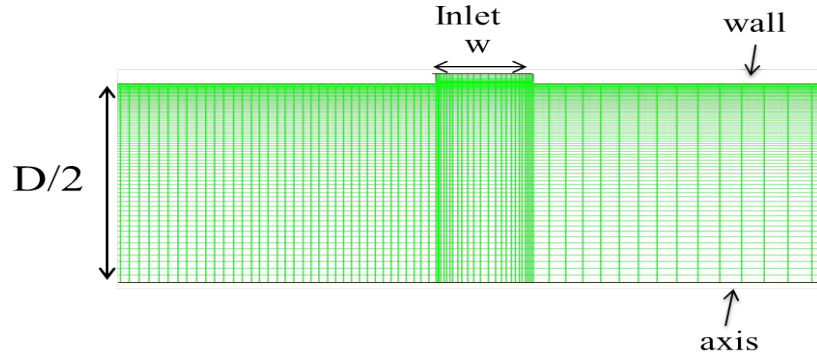
A cylindrical pipe domain was chosen for modeling long horizontal wells. An axisymmetric domain was used for 2D simulations. The perforation stages were modeled using annular inlets on the pipes. One such inlet represents a cumulative flow from all perforations in one zone and flow from each perforation was not simulated individually for the 2D simulations.

Figure 3.1a shows a schematic of the axisymmetric pipe domain used for 2D simulations. An axisymmetric pipe domain was chosen for simulations that constitute a part of this thesis. The domain is similar to the one used by Jha (2011) with some modifications. The diameter was chosen as $D = 0.127m$ which is a commonly used pipe size in the industry for wellbore applications. At the right end of the domain a wall boundary condition was imposed which represents the toe end of the well from which no flow was expected. The top boundary was modeled as the pipe wall with no flow. Five cross-flow inlets were modeled on the pipe wall as shown in Fig.3.1a and indicated by I_1 through I_5 . Here a total pressure boundary condition was used.

For time-dependent simulations the pressure is varied as a linear function of depleting reservoir volume, V_{init} , that is modeled. With flow rate from the inlets, the



(a) 2D axisymmetric geometry



(b) Close up of a crossflow inlet

Figure 3.1: Schematic of 2D geometry with five crossflow inlets and relevant dimensions.

reservoir volume decreases resulting in decrease of pressure, given by

$$P(t = 0) = V_{init}, \quad P(t) = f(V), \quad (3.1)$$

where V is the volume remaining in the reservoir at time t . Appendix D gives a user defined function describing how this function was applied in FLUENT using a subroutine.

The distance between each inlet was chosen to be $40D$. The last inlet near the toe, I_5 was at a distance of $0.5D$ from the toe. The left side of the domain was modeled as a pressure outlet boundary, chosen to be atmospheric. The bottom boundary of the domain is an axis, which gives the advantage of simulating flow in a pipe using rotational symmetry. Using a 2D domain, however, does not allow modeling the discrete perforation geometry. The inflow boundaries can be considered as a set of

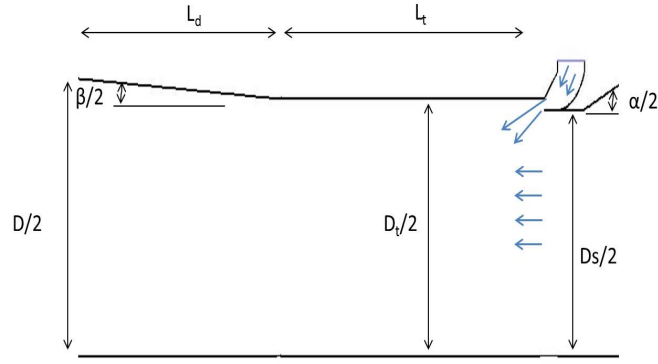
such perforations issuing flow into the horizontal well.

The domain was discretized into 2D elements using the Ansys meshing program. Figure 3.1b shows a close up view of the mesh near a cross-flow inlet. The inlet width is indicated by a reference value $w = 0.0125m$. A finer mesh near the pipe wall was used to resolve high spatial gradients near the no-slip boundary. Also, finer mesh was used near the inflow points with 30 times larger mesh separation in the axial direction away from the mixing area than near the inflow zone. The mesh density downstream of the inlet 1 and 2 was kept double than downstream for the other three inlets to resolve the turbulent flow that was expected in these regions. The results for the three different mesh resolutions are presented in the next chapter, to obtain mesh independence.

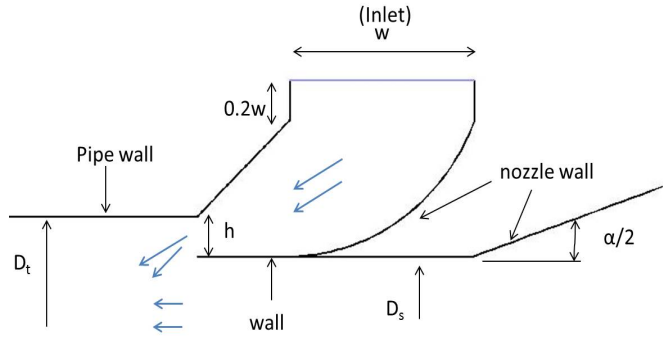
3.1.2. Two dimensional axisymmetric pipe domain with nozzles at inlets

To more accurately control flow from the inlets and avoid mixing losses at the same time, a nozzle configuration was employed at the inlets as shown in Figure 3.2. The inlet width on the main pipe remained the same. Only the geometry and corresponding mesh near the nozzle and in the nozzle cavity was changed.

The nozzle consisted of a converging section upstream of it that allowed laminar flow before injection and no recirculation to occur. The nozzle has a small opening h through which the flow entered the domain. The upstream flow enters the mixing region through a converging section that lead to a decreased diameter $D_s = 55mm$. The mixing throat region had a diameter $D_t = D_s + h$. This was followed by a gradually diverging section for pressure recovery and finally the straight pipe section. The converging angle was $\alpha \approx 37.5 \text{ deg}$ while the diverging section angle $\beta \approx 5.5 \text{ deg}$. The throat length was $L_t = D$ and diffuser length $L_d = D$. This design was derived from the annular jet pump configuration discussed in detail in the work of Shimizu et al. (1987) and Long et al. (2012). The present design might be improved further to reduce the losses due to flow through the nozzle. The throat and diffuser help to



(a) 2D axisymmetric geometry

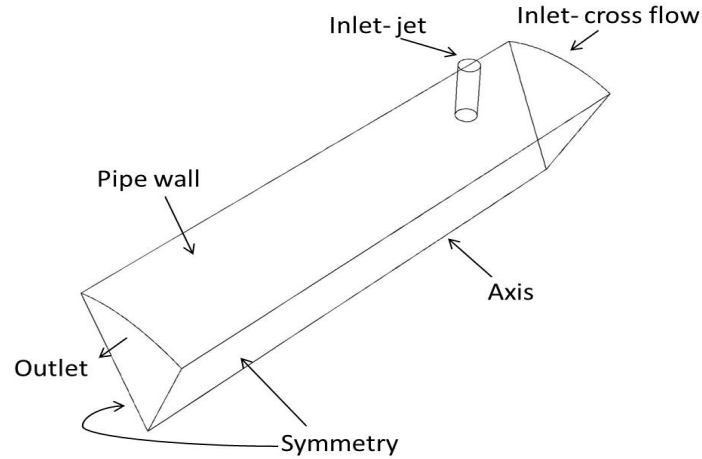


(b) Close up of a crossflow inlet

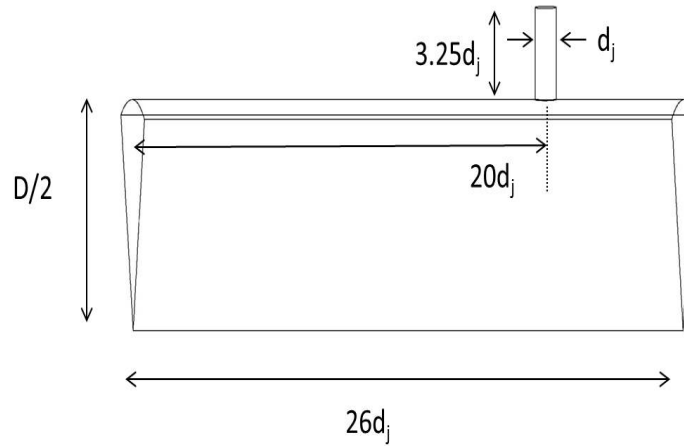
Figure 3.2: Schematic of 2D axisymmetric configuration with nozzle geometry on an inlet for modifying flow entry.

minimize flow reversal and enhance momentum transfer between the two streams.

The mesh resolution away from the nozzle entry area was similar to that used for the 2D axisymmetric geometry. Near the nozzle, a slightly finer mesh was required to get a converged solution for the simulated Re . Hence the mesh used for this geometry had 230,000 mesh elements. The nozzle opening h had 25 points across it with spatial variation having finer mesh towards the two wall boundaries. The mixing zone immediately downstream of the nozzle exit had the finest resolution. Also, the mesh density downstream of the inlets 1 and 2 was kept about 50% higher than near inlets 3, 4 and 5.



(a) Computational domain with boundaries



(b) Dimensions

Figure 3.3: Schematic of 3D geometry of a pipe with a nozzle.

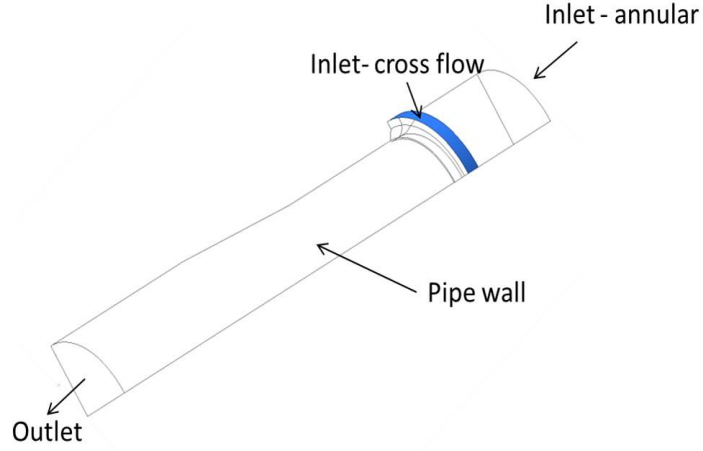
3.1.3. Three dimensional combustor geometry

Figure 3.3 gives a schematic of the three dimensional geometry of a pipe with an inlet injecting flow perpendicular to the pipe axis. This geometry resembled closely the combustor geometry used by Prière et al. (2005), with minor modifications. The diameter of the pipe was chosen to be $D = 100mm$, the same as their experimental setup and the jet diameter was chosen as $d_j = 6.1mm$. Figure 3.3a shows the boundary conditions used for the simulation conducted using this domain and Fig.3.3b shows the other relevant dimensions. As with Prière et al. (2005), the domain that

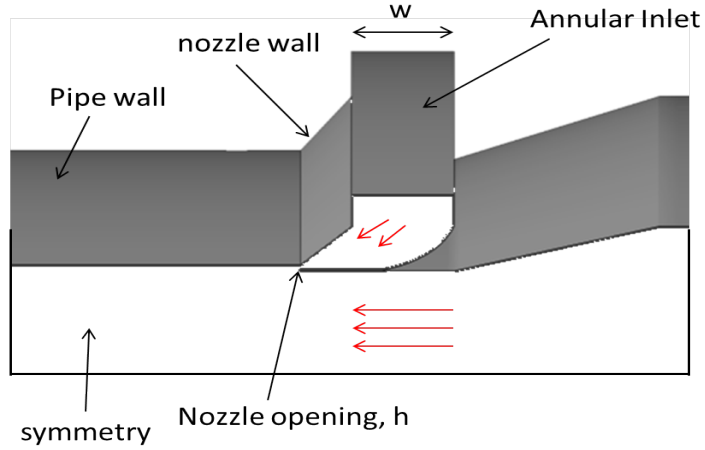
was used was a 45° cross section of the pipe and used symmetry boundary conditions on two sides as shown in the figure. A velocity inlet boundary condition was specified at the cross-flow and injection inlets. The outlet was modeled as a convective (out-flow) boundary. Two different meshes were tested against the experimental results of Prière et al. (2005). A hybrid structured-unstructured mesh was used here to allow mesh generation near the injection inlet. Mesh 1 had 0.4 million elements while mesh 2 consisted of 1 million elements. The mesh density was highest near the injection point where the two streams mix with each other. The mesh resolution near the wall was the finest, getting coarser towards the axis. Similarly the mesh resolution decreased going from the injection point towards the outlet and inlet. For mesh 1, at a $Re = 5.45 \times 10^5$ at the outlet, the y^+ value was 5.5 while at $Re = 5700$, $y^+ \approx 0.3$. Similarly, for mesh 2, for $Re = 5.45 \times 10^5$, $y^+ \approx 2.8$ and for $Re = 5700$, $y^+ \approx 0.14$ at the outlet, using the bulk average velocity at the outlet and the pipe diameter as the velocity and length scales.

3.1.4. Three dimensional nozzle geometry

Figure 3.4a shows a schematic of the three dimensional nozzle geometry used for simulating flow near a single inlet zone. As indicated in the figure, the main inlet remained the same as in previous cases, having diameter D of the pipe. The injection inlet is a circumferential inlet on the pipe wall. This geometry is a 3D revolution of the planar domain used in section 3.1.2. The flow enters the domain from the main cross-flow inlet and also the annular injection inlet. Unlike the previous section 3.1.3 where the inlets were discrete 90° jets with flow into the main crossflow, this geometry allows fluid from the annular inlet to have much more axial momentum than radial for the inflow. As with the 2D nozzle geometry, a mixing throat area and a diffuser section was considered.



(a) Isometric view of annular nozzle



(b) Close up of the annular inlet

Figure 3.4: Schematic of 3D domain with nozzle geometry installed on a single inlet.

3.2. Governing equations

The mass and momentum equations in differential form (together known as the Navier-Stokes equations) are

$$\frac{\partial u_i}{\partial x_i} = 0 \quad \text{and} \quad (3.2)$$

$$\frac{\partial u_i}{\partial t} + u_j \frac{\partial u_i}{\partial x_j} = -\frac{1}{\rho} \frac{\partial p}{\partial x_i} + \nu \frac{\partial^2 u_i}{\partial x_j \partial x_j} + f_i.$$

In the above equations, $\mathbf{u} = u(x, y, z, t)$ is the velocity field, ρ is the density

(constant for incompressible flows), p is the static pressure and f_i is any body force or momentum source terms. The subscripts i and j take on the values 1, 2 and 3 for the three spatial dimensions.

For tracking the transport of a passive scalar quantity, one extra equation per scalar is solved. This equation is

$$\frac{\partial \rho \phi_n}{\partial t} + \frac{\partial}{\partial x_i} (\rho u_i \phi_n - \kappa_n \frac{\partial \phi_n}{\partial x_i}) = 0, \quad n = 1, \dots, N, \quad (3.3)$$

where κ_n is the diffusion coefficient of the k^{th} scalar. The scalar is used to track and visualize a certain stream of fluid if mixing takes place between multiple streams.

3.2.1. Turbulence Modeling

At high Reynolds numbers (typically ≥ 2200 for pipe flows) the flow becomes turbulent. The mesh resolution required to resolve all the important scales in space and time for such flow can become computationally expensive. As an alternative turbulence modeling is generally adopted.

Turbulence modeling requires decomposition of instantaneous flow variables in the Navier-Stokes equations (Equation 3.2). For example, the i^{th} velocity component $u_i = U_i + u'_i$. Here, U_i is the mean (time-averaged) and u'_i is the fluctuating part of the instantaneous velocity u_i . Using this *Reynolds decomposition*, the Reynolds-averaged Navier Stokes (RANS) equations for turbulent flows can be written as

$$\begin{aligned} \frac{\partial U_i}{\partial x_i} &= 0 \\ U_j \frac{\partial U_i}{\partial x_j} &= \frac{1}{\rho} \frac{\partial}{\partial x_j} [-P \delta_{ij} + 2\nu S_{ij} - \overline{u'_i u'_j}] + F_i, \end{aligned} \quad (3.4)$$

where $S_{ij} = \frac{1}{2} \left(\frac{\partial U_i}{\partial x_j} + \frac{\partial U_j}{\partial x_i} \right)$ is the mean rate of strain tensor. ρ is the fluid density, P is the mean pressure, δ_{ij} is the Kronecker delta, ν is the fluid kinematic viscosity and F_i is the body force. Closure is achieved by modeling the Reynolds stress $\overline{u'_i u'_j}$,

generally using the eddy viscosity concept and Boussinesq hypothesis:

$$-\overline{\rho u'_i u'_j} = \tau_{ij} = 2\mu_t \left(S_{ij} - \frac{1}{3} \frac{\partial u_k}{\partial x_k} \delta_{ij} \right) - \frac{2}{3} \rho k \delta_{ij}, \quad (3.5)$$

where $k = \frac{1}{2} \overline{u'_i u'_i}$ is the turbulent kinetic energy and μ_t is the turbulent viscosity. For more details the reader is referred to Tennekes and Lumley (1972).

3.2.2. $k - \epsilon$ model

The $k - \epsilon$ turbulence model was used for all turbulent flow situations presented in this work. This model was chosen based on the validation tests for the case of flow from a jet issuing in a pipe for a range of Re . The results were compared against the experimental data of Yuan et al. (1997). Details of this validation process are available in Appendix C.

The transport equations for turbulent kinetic energy k and its rate of dissipation, ϵ , are given as

$$\frac{\partial(\rho k)}{\partial t} + \frac{\partial(\rho k u_i)}{\partial x_i} = \frac{\partial}{\partial x_j} \left[\left(\mu + \frac{\mu_t}{\sigma_k} \right) \frac{\partial k}{\partial x_j} \right] + 2\mu_t S_{ij} S_{ij} - \rho \epsilon \quad \text{and} \quad (3.6)$$

$$\frac{\partial(\rho \epsilon)}{\partial t} + \frac{\partial(\rho \epsilon u_i)}{\partial x_i} = \frac{\partial}{\partial x_j} \left[\left(\mu + \frac{\mu_t}{\sigma_\epsilon} \right) \frac{\partial \epsilon}{\partial x_j} \right] + C_{1\epsilon} \frac{\epsilon}{k} 2\mu_t S_{ij} S_{ij} - C_{2\epsilon} \rho \frac{\epsilon^2}{k}. \quad (3.7)$$

Here μ_t represents eddy viscosity,

$$\mu_t = \rho C_\mu \frac{k^2}{\epsilon}. \quad (3.8)$$

The default model constants in Fluent were used for all simulations as listed below. $C_\mu = 0.09$; $\sigma_k = 1.00$; $\sigma_\epsilon = 1.30$; $C_{1\epsilon} = 1.44$; $C_{2\epsilon} = 1.92$.

The enhanced wall treatment option in Fluent was used to resolve the velocity gradients in the wall boundary layer. This allowed the near-wall mesh spacing to be larger than otherwise would have been required to get an accurate converged solution.

3.3. One dimensional friction factor model

For flow in a straight pipe with smooth wall friction factor is a function of Reynolds number ($Re = \frac{\rho U D}{\mu}$), given as

$$f = 64/Re \quad (\text{laminar}, Re < 2200) \quad \text{and} \quad (3.9)$$

$$f = (100Re)^{-0.25} \quad (\text{turbulent}, Re \geq 2200). \quad (3.10)$$

Here U is the average velocity at any cross section. This relation was used to prescribe a pressure drop between two inlets in the horizontal pipe to account for long axial separations seen in actual wells. The pressure drop can be obtained as

$$\Delta p = f \frac{1}{2} \rho U^2 \frac{L}{D}, \quad (3.11)$$

where L is the separation distance. This model was applied at a sufficient distance downstream of the inlets so that a spatially steady axial-velocity profile was obtained. This was done to ensure that the pressure drop did not have any effect on the turbulent mixing process near the inlet or the velocity profile.

3.4. Numerical Method

Equation 3.2 were solved using the Semi-Implicit Method for Pressure Linked Equations (SIMPLE) algorithm (ref. Ferziger and Perić (1996)). For pressure interpolation, a second order central differencing scheme in FLUENT was used to get the face pressure on the volume elements from the cell-center values. The second order upwind scheme was used for discretization of momentum. A second order upwind scheme was also used for discretization of k and ϵ or ω equations as well. For unsteady cases the second-order implicit method was used. Details of each method can be found in (ref. ANSYS (2014)). ANSYS-Fluent uses a collocated scheme in which

pressure and velocity are both stored at cell centers. For calculation of the gradients from the cell-centered values, the Least squares method was used.

4. Results and Discussion

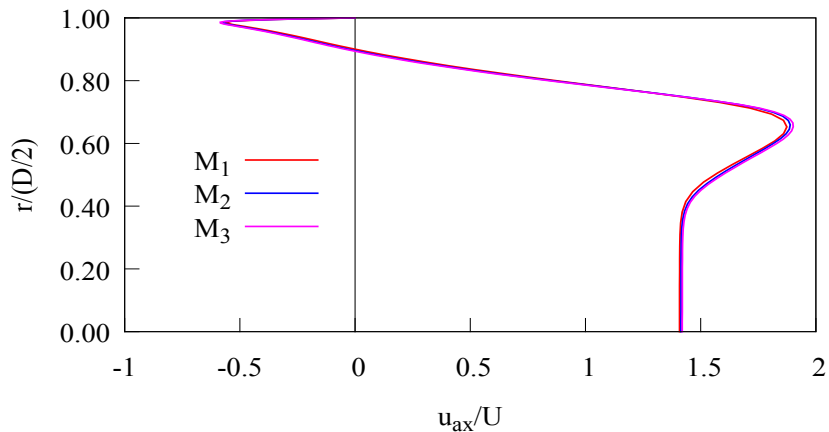
Results of simulations performed using the two-dimensional axisymmetric pipe domain with five cross-flow inlets will be discussed first. Using the pressure drop model discussed in Chapter 3 the long axial distances between two inlet zones can be taken into consideration. For unsteady cases, a time-dependent boundary condition is prescribed in the form of total pressure at the inlets. This initial pressure is a linear function of arbitrary volume, and the same BC is prescribed on all inlets. With flow into the wellbore the reservoir volume is reduced, thus, decreasing the pressure on the boundary. The BC is applied in Fluent using a User Defined Function (ref. Appendix D).

Properties relevant to those for crude oil were used for these simulations. A density of 850 kg/m^3 and viscosity of $0.003 \text{ kg/m} \cdot \text{s}$ was chosen to approximate crude oil properties. The initial pressure in the reservoir was fixed at 500 Pa. The $k - \epsilon$ model was used to model the expected turbulent pipe flow with high Re (> 2200), starting with an initially quiescent fluid.

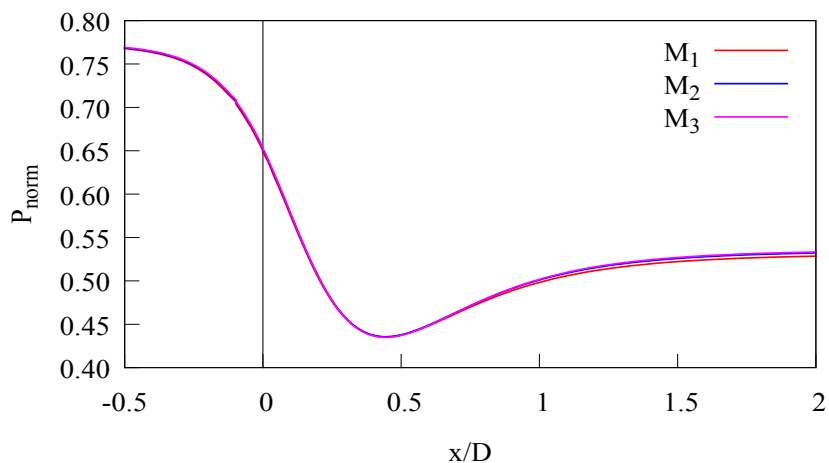
4.1. Mesh resolution

Three different mesh resolutions were tested for accuracy for the two-dimensional axisymmetric geometry. M_1 corresponds to a mesh with 70,000 elements, M_2 had 175,000 elements and M_3 had 200,000 elements. Across the radius of the pipe M_1 had 50 mesh points, M_2 had 75 points and M_3 had 90 points. Between M_2 and M_3 the axial direction resolution near inlet zones 1 and 2 was also increased. For these cases the Reynolds number based on bulk average velocity at the outlet and pipe diameter was 15000. Wall y_+ values near the outlet for mesh M_1 , M_2 and M_3 were 1.2, 0.6 and 0.5 respectively.

Figure 4.1 shows the velocity profile on a radial surface at a distance $x = 2w$



(a) Flowrate



(b) Total pressure along axis

Figure 4.1: Comparison between three different mesh resolutions for 2D axisymmetric domain.

downstream of the first inlet. This location was chosen because the maximum flow rate occurs after the first inlet and closer to the heel. The Reynolds number was maximum here and hence the mesh should be fine enough to resolve the flow features in this region. Also, the location was close to the inlet and the mixing process occurs here. This is evident from the velocity profile which shows a negative value of the axial velocity very close to the pipe wall. It was found that there was not much difference between the three mesh results for the axial velocity profile. On closer observation, there was found to be slight difference between the three meshes near $r/(D/2) = 0.6$.

Based on the observation that mesh 2 and 3 do not show much difference, mesh 2 was chosen for all further cases. Similar observations can be made from Figure 4.1b that shows the pressure profile on the axis near the first inlet. The location $x = 0$ in this case corresponds to the leading edge of the inlet. All three mesh give similar results. Thus the axial direction mesh spacing was considered sufficient for the simulated Reynolds number. Also, it should be kept in mind that the $\kappa - \epsilon$ turbulence model was used for the test. The results could not be compared against experimental or DNS results due to unavailability of any such database for the geometry considered here.

4.2. System in steady state

In this section we present results from simulations performed with different boundary conditions. Table 4.1 lists the different cases. The inlet size for each inlet is specified as a multiple of axial width w of the circumferential inlet, where $w = 0.0125m$. The initial reservoir volume V_{init} for each case is specified as a multiple of an arbitrary value V but corresponds to the same initial pressure for all cases. The draining of this volume into the well was simulated to study time-dependent behavior of the system with changing pressure and results are presented in section 4.3. Cases 1, 4 & 7 and cases 2 & 5 had the same inlet sizes on all inlets but the initial volumes were changed. Cases 1, 2 & 3 and cases 4, 5 & 6 had the same initial volume V but the inlet sizes were changed. Case 3 & 6 had inlet sizes increasing with distance from the heel to allow for the extra frictional pressure loss.

4.2.1. Relative pressure drop

Authors such as Ouyang et al. (1998) and many others have looked at perforated pipes and inflow from such wall perforations mixing with crossflow in a pipe. Frictional pressure losses have been studied for such setup. The frictional losses for the setup used in the current case is compared with that of Ouyang et al. (1998), who proposed

Table 4.1: Transient simulation cases using 2D axisymmetric geometry.

Case	Inlet size					V_{init}
	I_1	I_2	I_3	I_4	I_5	
1	w	w	w	w	w	V
2	0.2w	0.2w	0.2w	0.2w	0.2w	V
3	0.1w	0.15w	0.25w	0.40w	w	V
4	w	w	w	w	w	0.2V
5	0.2w	0.2w	0.2w	0.2w	0.2w	0.2V
6	0.1w	0.15w	0.25w	0.40w	w	0.2V
7	w	w	w	w	w	10V

the analytic expression

$$f = f_0 (1 + 0.0153 Re_w^{0.3978}), \quad (4.1)$$

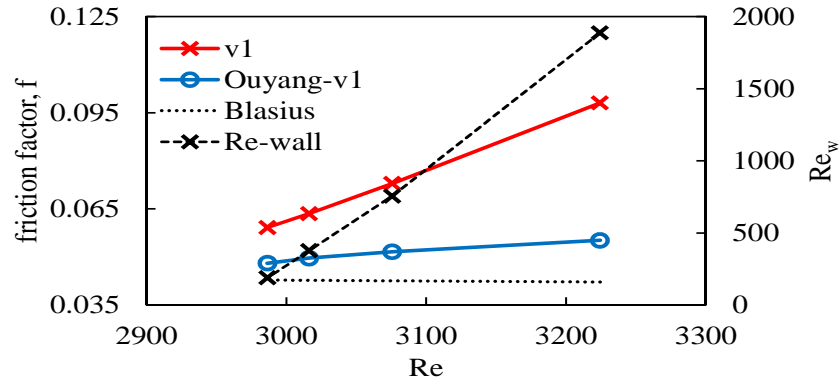
where f_0 is the friction factor with no inflow from the wall and Re_w is the Reynolds number for the wall inflow based on pipe diameter and inflow average velocity.

For the purpose of comparison case-2 from Table 4.1 was chosen as a reference. The inlets were given a prescribed velocity inflow condition. The inflow based Re_w along with friction factor f is plotted against the total flow (downstream) Re for inlets 1 through 4 in Figure 4.2. Two cases v1 and v2 were chosen. The cross-flow specified for the two cases was different, as observed from the plots for low and high Re ranges. There is some difference between the simulation results and the Ouyang model. The analytical model was proposed for lower Re_w range. Hence, better agreement with the model is observed for the lower Re_w case. The basic trend was similar between the model and simulation. It is interesting to notice that the Blasius friction factor, shown for reference here, decreases with increase in Re . But with inflow from the wall, the velocity profile changes near the inlet zones and turbulence mixing takes place which results in a higher pressure loss. The geometry used for the simulation is different than the experimental results that were the basis for the model. The difference in

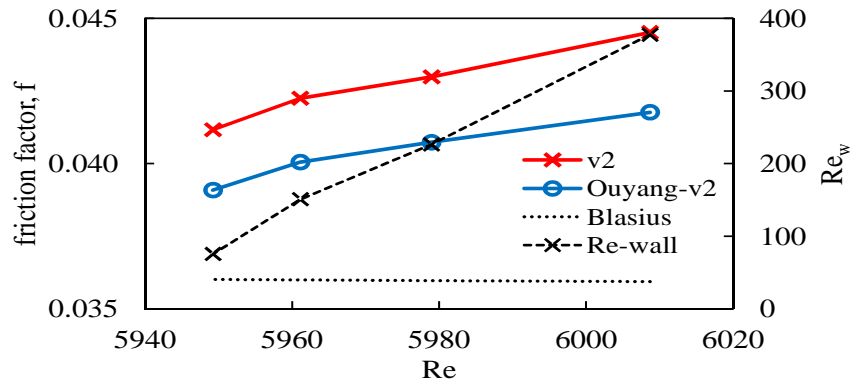
friction factors can be attributed to this. Also, the simulated cases have higher inflow to main flow rate ratio whereas the experiments were conducted for $Re/Re_w < 0.01$. This influenced the results too. Nevertheless, the trends of friction factor and also relatively accurate values at lower Re_w justifies the use of the simulation setup.

4.2.2. Modeling inter-zone distance

The effect of distance between any two inlets is discussed here. The change in this inter-zonal distance was modeled using the principle of one-dimensional friction factor by changing L in Eqn. 3.10. The pressure at the inlets was fixed at 500 Pa and steady state simulations were performed using the setup of case 1 from Table 4.1. Figure 4.3a compares the flow rate from each inlet for three different axial separation

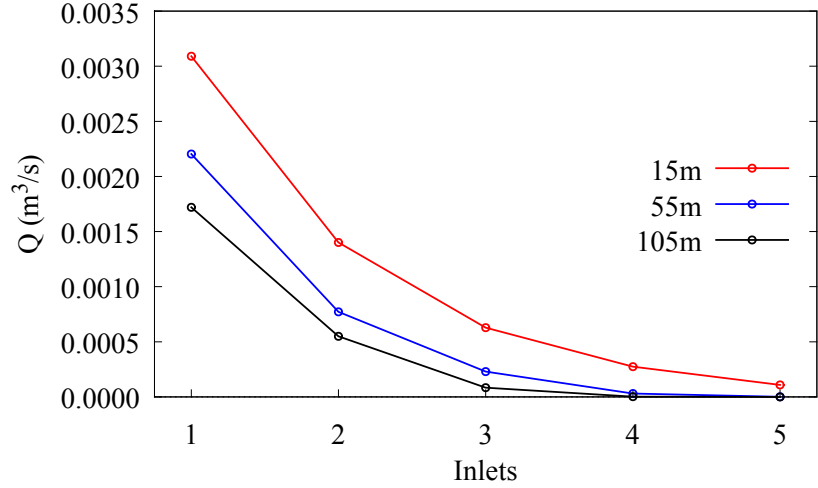


(a) Low Re

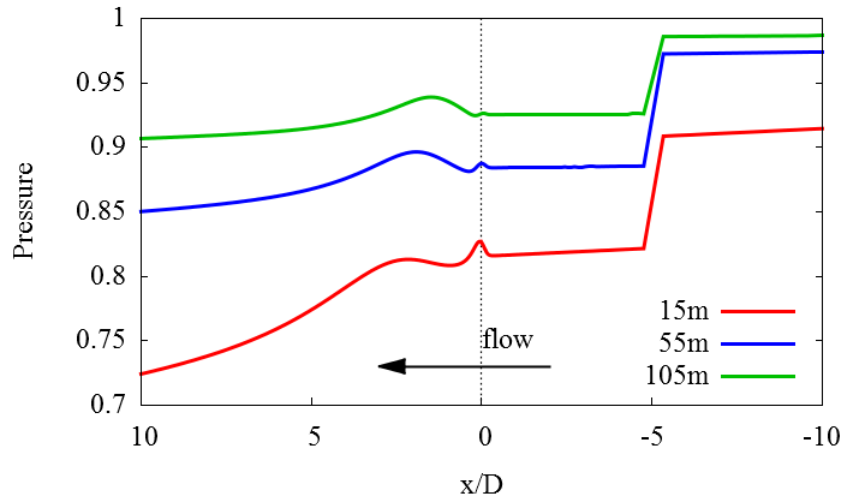


(b) High Re

Figure 4.2: Friction factor comparison for wellbore flow with Ouyang et al. (1998) model.



(a) Flowrate



(b) Total pressure along axis

Figure 4.3: Comparing flow rate and pressure profile along the well length for different axial separation between inlets.

cases between inlets. Figure 4.3b shows the total pressure on the axis of the pipe as a function of distance. The $x/D = 0$ axis represents the trailing edge (in the flow direction) of the first inlet.

It can be observed that by increasing the axial separation, the flow rate from each inlet decreased. This was due to added pressure loss prescribed by the model. For a separation distance of 15m the system was in *partially blocked* state where the inlets 4 and 5 near the toe were contributing small amounts to the total flow rate. With 55m

and 105m separations the toe inlets were completely *blocked*. The gradual removal of blocking effect can be observed with decreasing distance. But the shape of the flow-rate curve remained similar for all three cases. The total pressure along the pipe axis presented in Figure 4.3b shows the pressure drop before the first inlet where the 1D model is applied. Only a partial axial limits of the domain is shown here. For each case the pressure drop upstream of the first inlet was different. This resulted from the difference in cumulative flow rates upstream of the inlet. The variation in total pressure downstream of the first inlet was also observed that signified the variation due to mixing process between the cross-flow and Q_1 . After flow interaction between the two streams the pressure once again normalized and started decreasing linearly. It can be noted that the pressure drop model was applied at a location where there was a linear decrease in pressure. The flow had fully developed and the pressure gradient was constant downstream of the second inlet (not shown).

4.2.3. Effect of inlet size

The effect of inlet size on the production profile was studied by Jha (2011) for laminar flow in pipes. The results presented here extend that study into turbulent flow regime. Turbulence modeling was carried out using $k - \epsilon$ model and a distance of 105m was modeled between each inlet as discussed in the previous chapter.

Figure 4.4 shows the flow rate from individual inlets for cases 1, 2 and 3 with different inlet sizes. As observed from the red dotted curve, case 1 with large inlets shows *blocking effect* where only the first two inlets were producing nearly all the flow and the contribution from last three inlets was minimal. Hence, the red solid curve is flat from inlets 3 to 5. The blue curves for case 2 show nearly equal production from all the inlets, decreasing only slightly towards the toe due to added pressure drop from the model. The green color curves representing case 3 also behave similarly but the total production is lower than case 2. *Trickle flow* is evident here also but the inlets could be producing more. The inlet sizes increased from the heel towards the

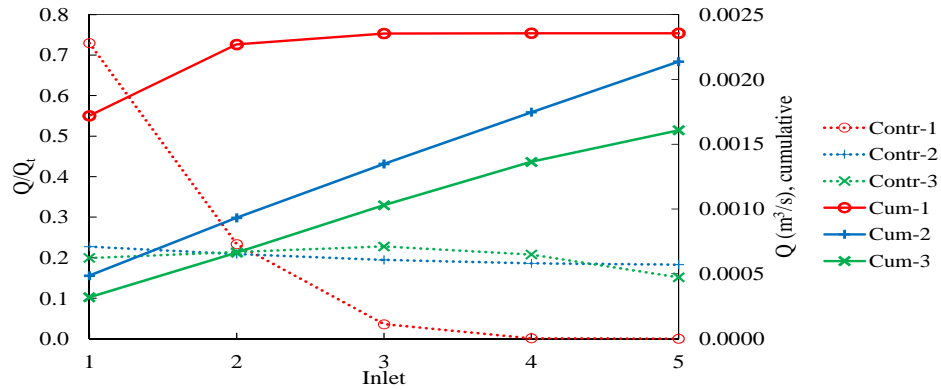


Figure 4.4: Steady state flow rates compared for Cases 1, 2 and 3. Dotted lines represent the contribution to total production Q_t for each case. Solid lines represent the cumulative flow wellbore rate starting from inlet 1 near the heel.

toe. The variation in the inlet sizes was such that the flow from each was restricted for the given pressure drop. Inlet 5 showed *partial blocking* where there is flow from the inlet zone, but it is restricted by the total flow from the downstream inlets.

The above analysis can be applied to the well log data shown in Fig. 1.2. The 30 day cumulative flow rate curve suggested a significant blocking effect, as in the large inlet-size *Case – 1*, for the inlets towards the toe end of the well, while the inlets towards the heel produce most of the total flow. The 155-day curve in Figure 1.2 corresponds to decreased inlet pressures near the heel as these reservoirs had drained, allowing the toe inlets which had higher pressure to overcome the decreased blocking effect of the heel inlets. Note that the total production level of the well had also dropped over this time period. This is similar to the small inlet-size *Case – 2* discussed above, where the system approaches a trickle flow regime, in which each inlet then produced independent of other inlets corresponding to the pressure gradient available to it.

4.3. Time dependent cases

As shown in Figure 1.2, the nature of the wellbore flow regime can change significantly over the production cycle of the well. The inlet size and pressure combine

to change the flow rate from each inlet and its corresponding flow regime. To investigate these effects related to reservoir depletion, several five-inlet simulations were performed using time dependent boundary conditions.

The following time-scales are relevant to this problem. The ‘equilibration’ time scale T_e is the time from initialization to establishment of a steady flow in the domain, with constant boundary conditions. The ‘flow’ or ‘draining’ time scale T_d is the time after equilibration during which significant reservoir depletion occurs. The separation of these two time scales is important (Ref. Jha (2011)), and was achieved by first establishing an equilibrated state. After a sufficient T_e , the time-dependent reservoir drainage was initiated. Once a steady production state is reached the system enters T_d . T_{eq} is not shown for any of the cases indicating that a steady state flow solution had been reached at the beginning of the time-dependent solution. Only T_d is the scale of interest in the present simulations and is shown for all cases. The initial reservoir volume V_{init} corresponds to the boundary condition used for steady state simulations.

Vicente et al. (2002) provide insight into time dependent change in flow regime, relating it to the pressure draw down and reservoir properties. Their research showed the presence of a blocking mechanism and its removal in time, albeit with a longer well length and porous inflow boundary conditions along the total length. In the present study, discrete inlet points, each corresponding to a completed perforation stage, along the wellbore have been used. The pressure at the inlet boundary varies with time as described below. Mass flow at the outlet is not prescribed, as in Vicente et al. (2002) and other studies in literature, but is determined by the simulation itself.

Linear pressure model: An inlet pressure boundary condition decreasing linearly in time was used to simulate the effects of reservoir depletion from flow entering into the wellbore through the cross-flow inlet. The inlet pressure, prescribed from a user defined subroutine, was assumed to be linear function of the remaining reservoir

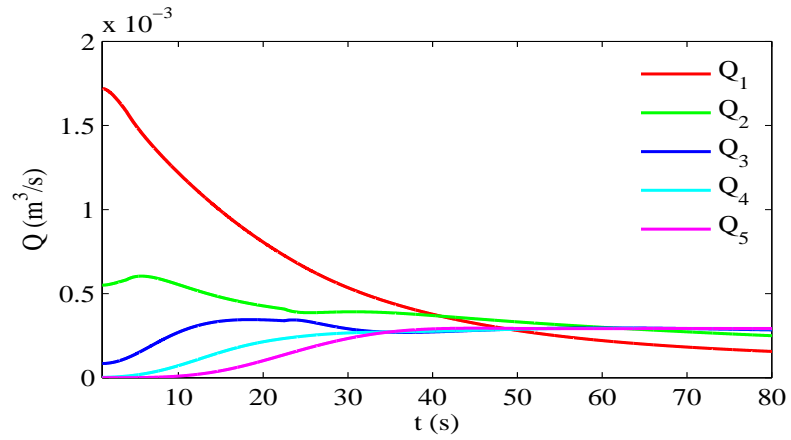
volume (after inflow into the pipe) at any given time. This simple linear model was used to study how the flow rate from each inlet depends on all the inlet pressures as well as downstream pressure gradient. Many different and more sophisticated reservoir models (e.g., Penmatcha and Aziz (1999), Vicente et al. (2002), etc.) are available and can be prescribed in place of the given model here. The coupling of such wellbore models with the CFD simulation and its subsequent analysis is not the objective of this work.

4.3.1. Effect of inlet size

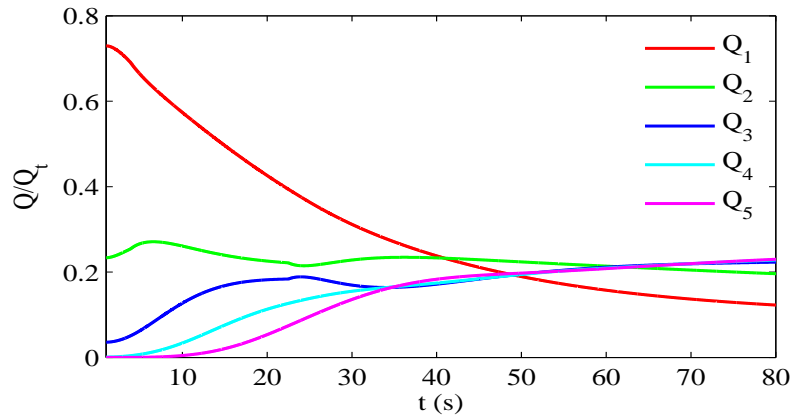
Case-1: Figure 4.5a shows change in flow rate for each inlet over time. Initially at $t = 0s$, Q_1 and Q_2 dominate the total flow with Q_3 also producing some flow, but Q_4 and Q_5 are blocked. This is evident from Fig. 4.5b which shows flow rates for individual inlets normalized by total flow rate for the system at the heel. Q_1 contributed nearly 70% of the total flow, with Q_2 nearly 25%. Over time the pressure at inlets near the heel decreased and the blocking effect weakened, thus allowing inlets 3, 4, and 5 to produce more flow. The removal of blocking effect is evident from Fig. 4.5c which shows the regime change of the system over time. At $t = 15$ blocking effect was evident, with first inlet producing most of the flow. At $t = 45$, all inlets were producing at approximately same rate.

Pressure on each inlet decreased with decrease in reservoir volume. Figure 4.6a shows the decreasing pressure (normalized by initial total pressure) on each inlet over time. The removal of blocking effect was attributed to the decrease in pressure on the first inlet which allowed other inlets to start producing. The time change of the drained volume for a reservoir section associated with each inlet is shown in Fig. 4.6b. At 70s flow time, nearly 70% of the initial volume in first reservoir section had drained, whereas that from the fifth inlet only reached little over 20%.

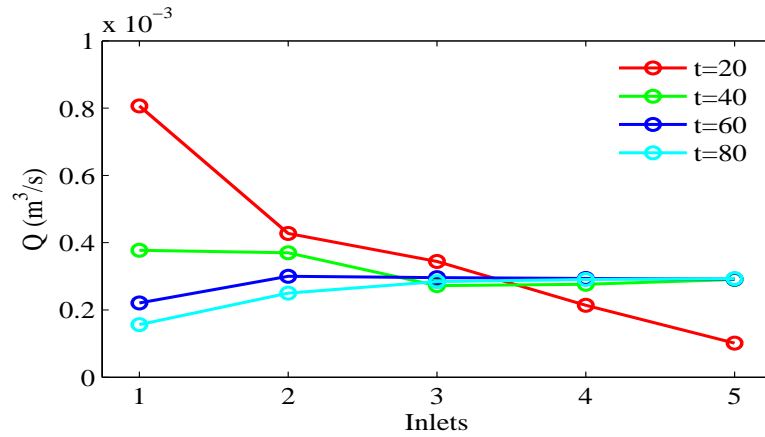
Cases 2 and 3: Inlet sizes were changed on all the inlets to $0.2w$ in case 2 and changed incrementally in case 3, as listed in Table 4.1. The simulations were repeated



(a) Flowrate

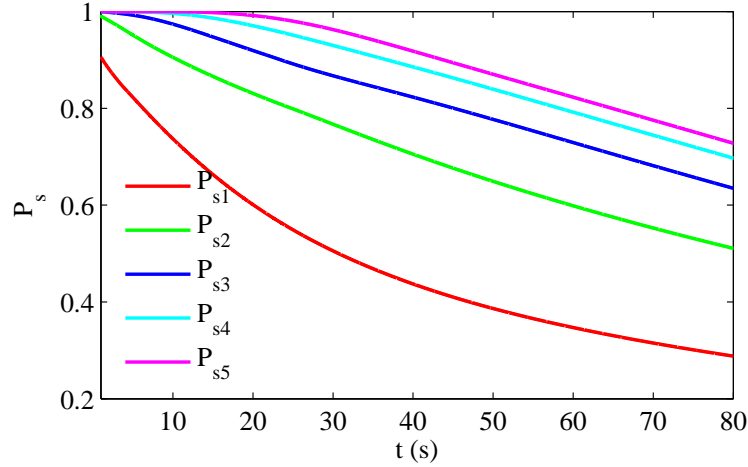


(b) Normalized flowrate

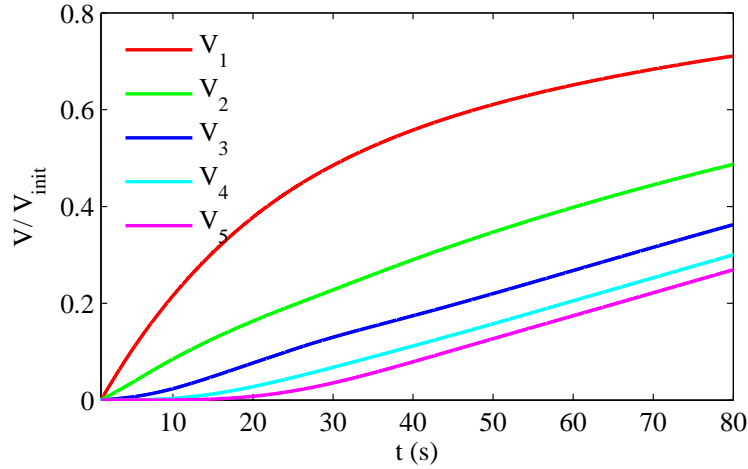


(c) Individual flow rate (Regimes)

Figure 4.5: Flow rate, normalized flow rate and flow-regime change over time for case 1 (Table 4.1)



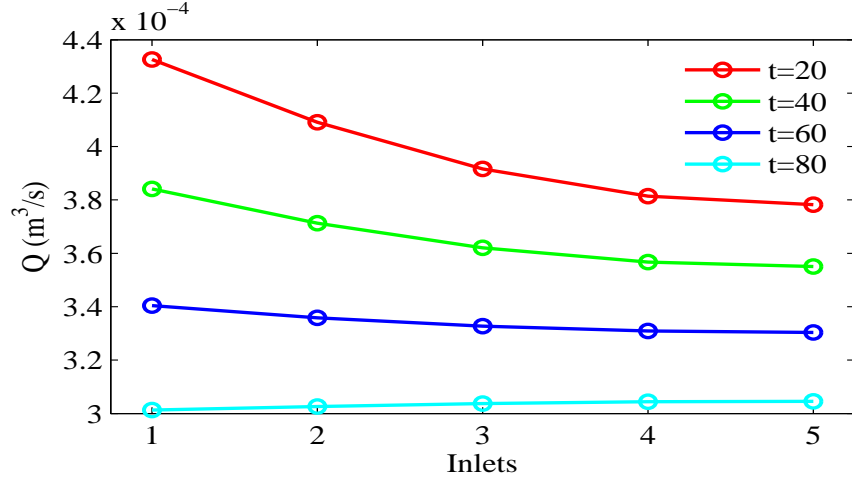
(a) Static pressure



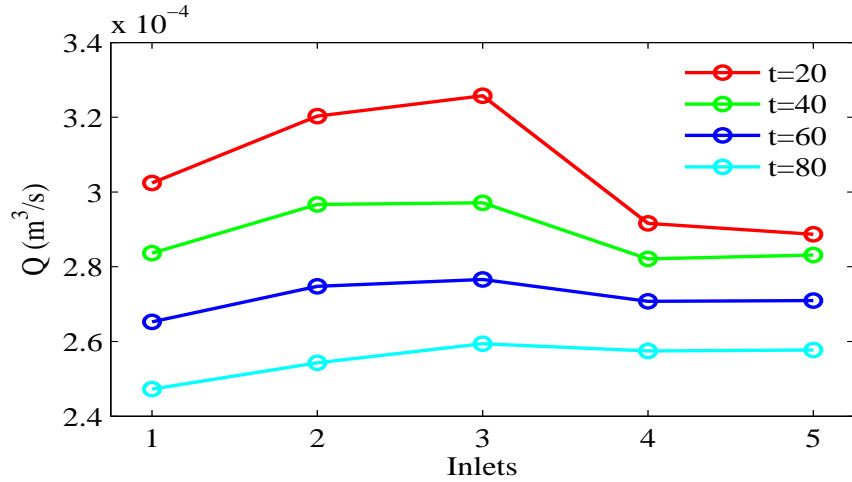
(b) Drained volume

Figure 4.6: Normalized static pressure and drained volume for case 1 (Table 4.1)

with same initial volume on each inlet. Figure 4.7 presents the regime change for the two cases with depletion of volume in time. Steady state analysis from Figure 4.4 showed that at $t = 0$ Case 2 was already in a *trickle flow* regime. The overall flow regime does not change much over the course of the simulated time. Case 3 also undergoes a similar change seen in Fig. 4.7b. Depending on the inlet size, the initial production from each inlet varied. But as the reservoirs depleted, the flow rates normalized. The system was in partial blocking initially, as will be explained from analysis of Fig. 4.8.



(a) Case 2



(b) Case 3

Figure 4.7: Regime change of system over time for cases 2 and 3.

The total flow rate for cases 1,2 and 3 are compared in Fig. 4.8. Case 1 with the largest inlets produced most flow at the start of the simulation. But the rapid decrease in pressure on the inlets near the heel lead to decreased production there. By $t=15$, case 2 was producing more flow than case 1. This shows that initially a well with large inflow zones produces more flow than another well with smaller inlets. But over the course of production time, the smaller inlet well could produce more flow. Some horizontal wells produce high flow rates initially and this could result from the initial domination by the heel inlets. But with reservoir depletion and the system moving toward trickle flow regime the advantage is lost. In such cases, smaller or

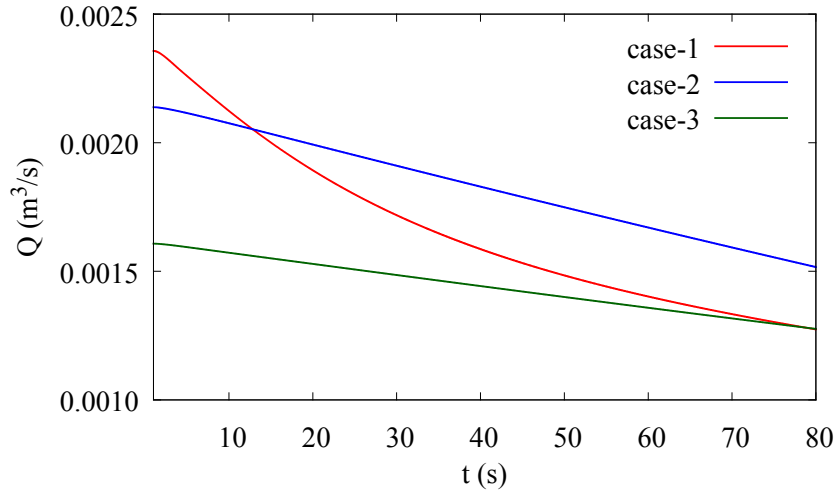
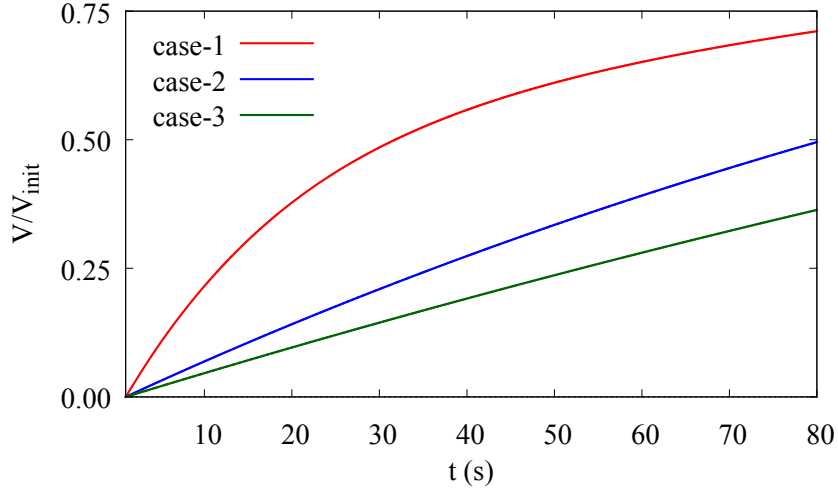


Figure 4.8: Total flow rate at the heel over time compared for cases 1, 2 and 3.

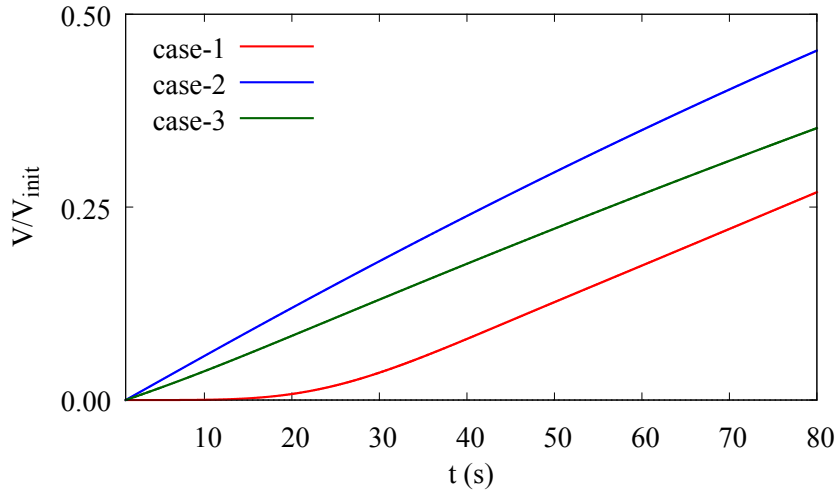
incremental inlets might be of interest.

For case 1, 2 and 3 the volume drained over time from the first and fifth inlets are shown in Figure 4.9. Over the course of simulation nearly 70% of the initial volume was drained out in case 1, while only about 50% was drained for case 2 and 30% for case 3. But due to initial blocking, the recovery from fifth inlet was better for cases 2 and 3 compared to case 1, as indicated by Fig. 4.9b. Case 1 could produce only about 25% of the initial volume from the fifth inlet, whereas case 2 produced about 45% and case 3 about 35%.

Initially, it can be argued that case-1 showed the maximum production of the three cases, but over time, the advantage was lost due to decrease in pressure. This behavior is significant and needs to be taken into account when designing a well. A higher initial flow rate might not necessarily give higher total production over an extended time period. Also, as discussed by Asheim et al. (1992), Oyeka et al. (2014), Halvorsen et al. (2013) and others, rapid decrease in pressure near the heel compared to the toe have a greater risk of premature water breakthrough which is undesirable. From our simulations such a situation is possible in case of large inlets exhibiting high flow rates from the heel region.



(a) Inlet 1



(b) Inlet 5

Figure 4.9: Volume drained over time from inlet 1 and 5 compared for case 1, 2 and 3.

The dependence of total production over time on inlet size was found to be very important. So, for completeness, this dependence is compared for various inlet sizes in Figure 4.10. At $t = 10$ the system with size w had drained more fluid than the other systems. But at $t = 30$ cases with both $0.2w$ and w inlet sizes had produced about same and at $t = 80$ the total volume drained from the $0.2w$ -case was higher than the large (w) inlet size. This reconfirmed that the inlet size that produced maximum flow rate initially was not suitable over the simulated time for maximum drainage. Also,

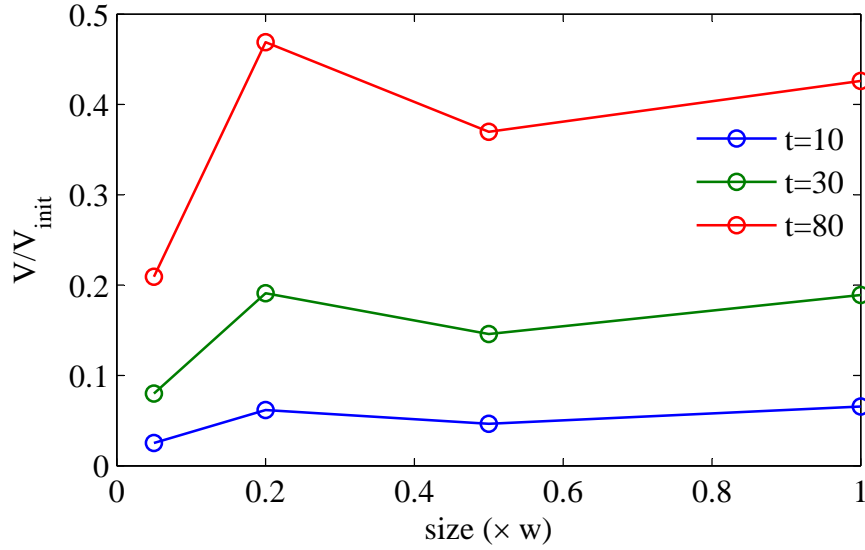


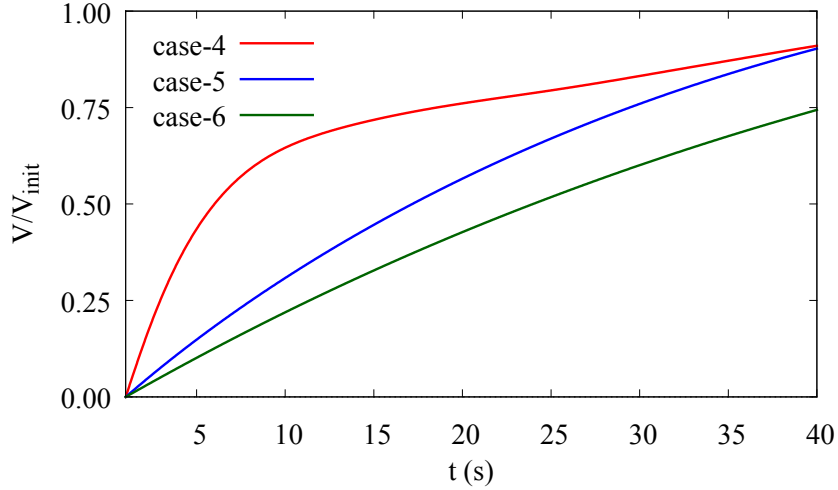
Figure 4.10: Total volume drained for systems with different inlet sizes.

at very low inlet size of $0.05w$ the total production was least of the sizes considered.

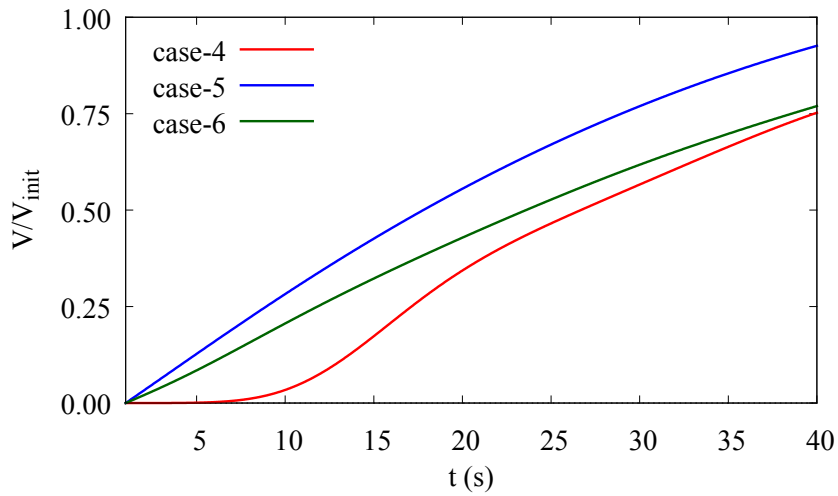
4.3.2. Smaller volume: Initial transients

Cases 4, 5 and 6 have smaller initial volume used for the time-dependent calculation. At $t = 0$, the boundary conditions are same as cases 1, 2 and 3 respectively. But starting with initially smaller volumes resulted in faster decrease in pressure on each inlet. The relative increase in flow rate was quicker than observed in cases 1, 2 and 3 and presented a transient effect that was not ideal for studying draining and its isolated effect on the system.

The volume drainage over time from the fifth inlet is shown in figure 4.11b. For the time period shown ($0 < t < 40$) volume drainage was considerable compared with the larger V_{init} cases. Over the same time period shown, case 2 setup (size = $0.2w$) was able to drain more volume from inlet 5 than the other two cases. Case 1 with large inlet setup and case 3 with incremental inlets were able to drain about the same volume but initially, case 3 produced more flow, as was shown in Fig. 4.9b. So if the time scale for production was kept short, case 3 would have produced more flow from the toe inlet. Although the initial pressure was the same as other cases the total



(a) Inlet 1

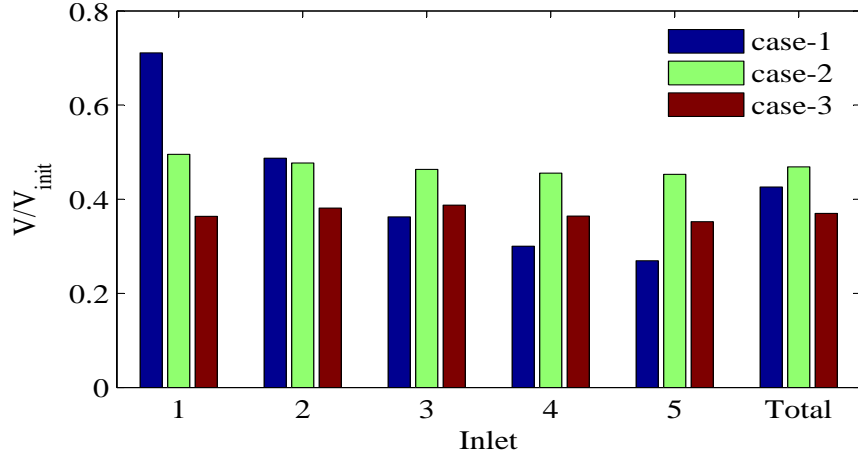


(b) Inlet 5

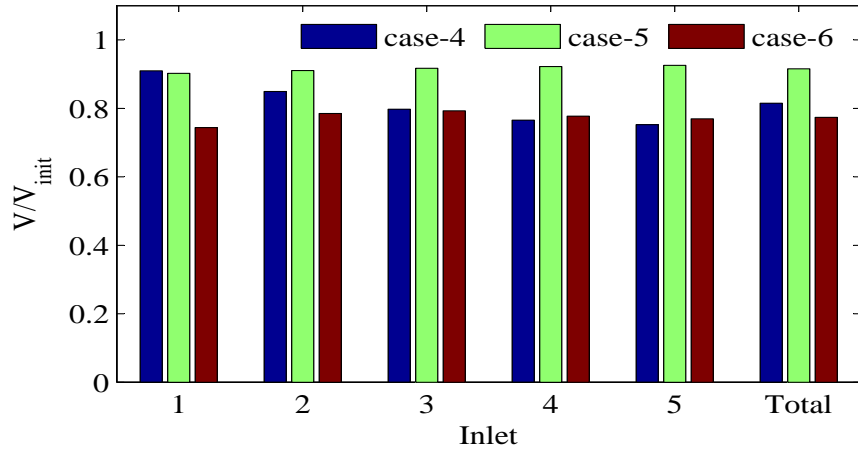
Figure 4.11: Comparison of drainage from inlet 1 and 5 for cases 4, 5 and 6.

drainage was less efficient due to the low flow rates from all inlets.

Figure 4.11b compares volume drained from the fifth inlet near the toe for cases 4, 5 and 6. The initial volume in these cases being lower than cases 1, 2 and 3 respectively, the drainage is quicker as can be observed by comparing with Fig. 4.9b. All three cases showed drainage more than 75% for a simulated time of 40s than for 80s in the previous set of cases. Again, case 2 was more effective in draining the fifth volume than the other two cases, suggesting that the inflow area or the perforation



(a) Cases 1, 2 & 3, $t = 80s$.



(b) Cases 4, 5, & 6, $t = 40s$.

Figure 4.12: Fraction of initial volume drained from each inlet at $t=80s$ for Case 1, 2 & 3 and at $t=40s$ for Case 4, 5 & 6. Total drainage takes into account all individual volumes.

sizes would effect the total production from the toe-end stages.

Figure 4.12 shows the total volume drained from each inlet for the different cases as indicated. If cases 1, 2 and 3 are compared, inlet 1 is dominant for case 1. But with the fifth inlet being blocked for some duration, the reservoir volume at that inlet could not be drained effectively. The drained volume fraction decreased from heel towards the toe. Case 2 showed a very balanced production from all inlets and about 45% recovery from fifth. Case 3 also showed about same level of production from each

inlet, but less than case 2 suggesting that the inlet sizes were a limiting factor for the given pressure drop. The total volume recovered from each case suggests that among the three cases discussed, case 2 was the best configuration for maximum recovery of fluid from the reservoirs. Similar inferences can be made for cases 4, 5 and 6. Case 5 with smaller inlet sizes at all inlet points provided the best recovery of initial volume, compared with case 4 having larger (w) inlet size and case 6 having incremental inlet sizes, as described in Table 4.1. The blocking effect played an important part, as in case 4, where the due to initial high flow rate from inlet 1 near the heel, the other inlets had reduced contributions but were still losing pressure due to flow. On gradual removal of blocking, the inlets near the toe started to increase in contribution to the total flow rate, but already had reduced pressure. Case 2 (and 5) showed trickle flow regime initially which does not ensure the maximum flow rate from any inlet but the toe-inlets were not blocked and hence produced more flow over time.

4.3.3. Effect of Reservoir Volume

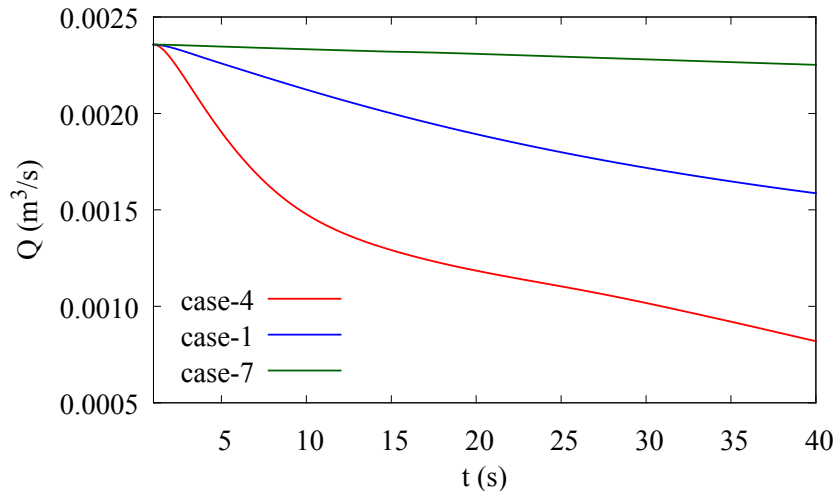


Figure 4.13: Total flow rate comparison for different initial volumes.

Flow rate at the heel is compared for cases 1, 4 and 7 in Fig. 4.13. These cases have the same inlet size (w) on all inlets with different initial volumes as listed in Table 4.1. Due to a high initial volume ($10V$) the decline of total flow for case 7

Table 4.2: Simulation cases with nozzles at inlets

Case	Nozzle size					V_{init}
	h_1	h_2	h_3	h_4	h_5	
JP-eq1	0.1w	0.1w	0.1w	0.1w	(w)	V
JP-eq2	0.2w	0.2w	0.2w	0.2w	(w)	V
JP-incr	0.1w	0.15w	0.25w	0.4w	(w)	V

is slower compared to the other two cases. For case 4, the decline was rapid as the volume was least of the three cases and, hence, the decrease in pressure on the inlets was also rapid. The slope of decline curve changed with time suggesting transient effects that occurred over the time period shown. This is likely due to the small reservoir size and relatively faster removal of blocking effect. Like case 7, case 1 also showed minimal transient effects for this time period but the decline from the initial reservoir volumes was significant. As this time period could be simulated, given the computational resources, this initial volume was chosen as the base case for detailed analysis described earlier.

4.4. Nozzles on inlets

This section describes the use of nozzles on the inlet zones to study their impact on decreasing the blocking effect. The objective was to increase production from the upstream inlets near the toe by homogenizing production from all inlets without having to change the inlet sizes on the pipe itself. This was achieved by modifying the entry of the flow from the circumferential inlet through a nozzle. The design of this nozzle was based on annular jet pumps as described in Shimizu et al. (1987). The design of the nozzle has been detailed in Chapter 3.

Table 4.2 lists the cases that were simulated. The first case *JP-eq1* has equal nozzle size of $0.1w$, *Jp-eq2* has nozzle size of $0.2w$ and *JP-incr* has progressively larger nozzle size from heel to the toe. Both cases had the same initial volume at $t = 0s$. For the three cases the fifth inlet that was closest to the toe did not have a

jet pump configuration on it and issued flow freely into the well like a regular inlet as in previous cases. In the absence of a cross-flow for the fifth inlet (the toe end was prescribed a no-flow boundary condition), the jet pump did not provide any advantage over a regular inlet. Hence, by not using a jet pump on the fifth inlet, the losses associated with flow through the jet pump itself could be avoided.

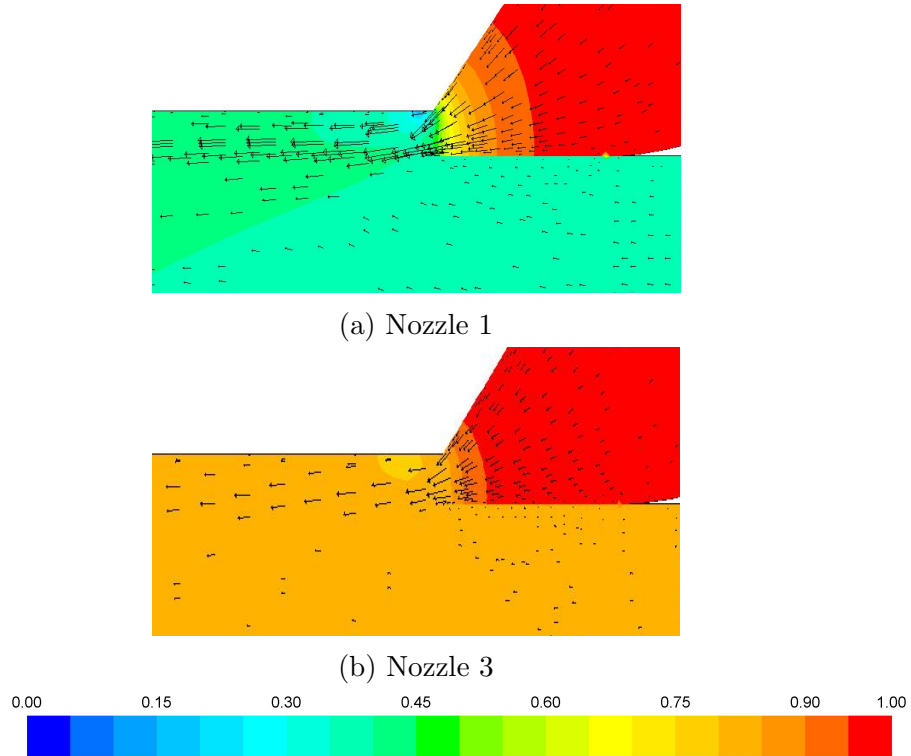


Figure 4.14: Velocity vectors overlaid on pressure contours near the jet pump nozzle for inlets 1 and 3 for *JP-eq1* case. The vectors are scaled (5x) and sampled ($x/5$). The colormap corresponds to normalized pressure contour.

Figure 4.14 shows the static pressure contours for *JP-eq1* case with velocity vectors overlaid, near inlets 1 and 3 at $t = 0$. The contour shows how most of the static pressure is trapped in the jet pump cavity due to the nozzle size being very small compared with the main inlet size. The pressure near the nozzle starts to decrease as it gets converted to dynamic pressure indicated by the vectors. Near nozzle 1 the upstream pressure is higher than for the upstream flow near nozzle 3 which is due to lower upstream flow rate from the toe stages. The velocity through the nozzle 1 is

higher than nozzle 3.

4.4.1. Steady state analysis - Flow regime

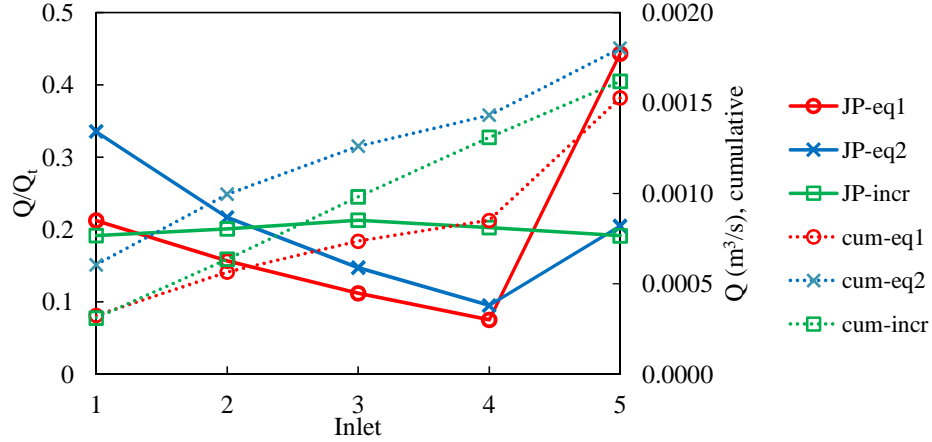


Figure 4.15: Steady state flow regimes for jet pump cases. Solid lines - relative contribution to total flow rate; dotted lines - cumulative production.

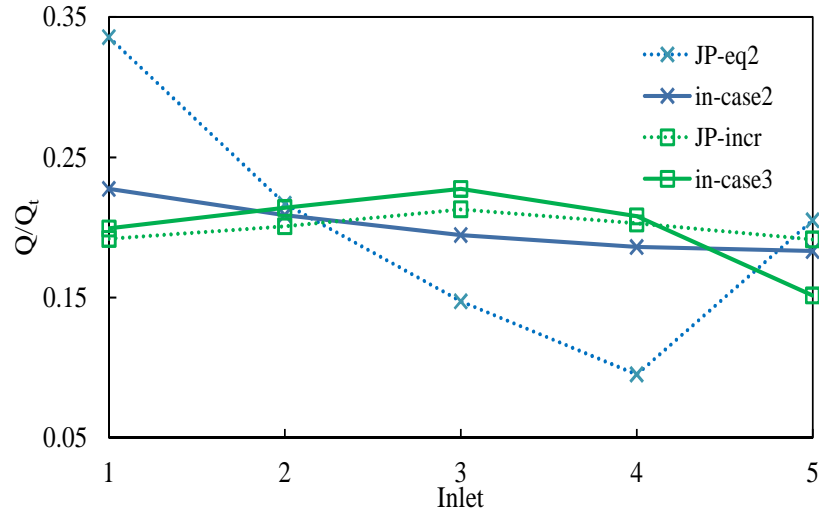
Figure 4.15 gives individual flow rate contributions and the cumulative flow rate from the heel to the toe, for steady state simulation of the three jet pumps cases. Here, a constant pressure boundary condition was prescribed on all inlets. It can be observed that *JP-eq1*, which had smaller nozzle size $0.1w$ on inlets 1 to 4 produced from all inlets close to *trickle* flow regime. The fifth inlet produced much higher flow than the other four inlets due to its relatively large size w . Similarly, for case *JP-eq2* the first four inlets produced in *trickle* flow but the fifth inlet produced nearly the same as second inlet. The first four inlets produced higher than *JP-eq1* case due to their $0.2w$ opening. This had an effect on relative *blocking* of the fifth inlet. Case *JP-incr* showed same relative contributions from all inlets. This was due to the increasing size of the nozzle opening towards the toe. The cumulative flow rate for the three cases are shown in dotted lines. Although the fifth inlet contribution for *JP-eq1* was the highest, it had the lowest cumulative flow rate due to the small nozzle sizes. *JP-eq2* produces the highest total flow rate whereas *JP-incr* case had slightly

lower total flow rate.

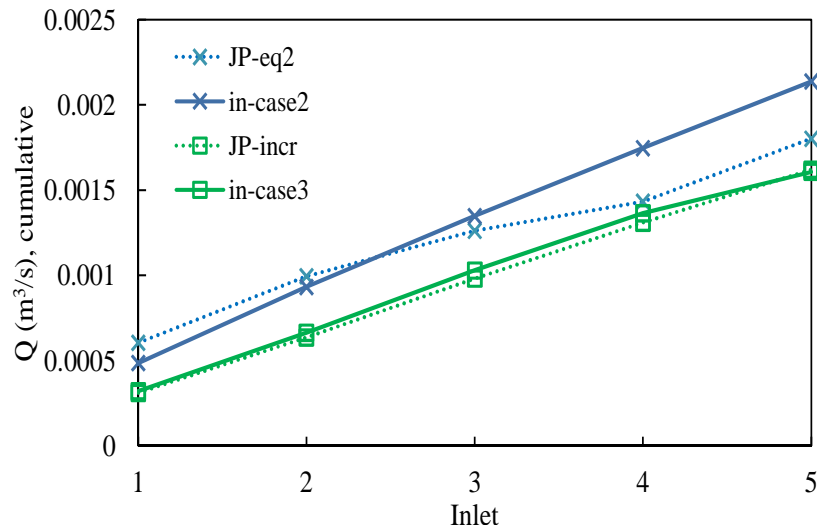
It is interesting to note here that the reservoir-wellbore coupled model of Vicente et al. (2002) predicted a similar flow rate distribution as *JP-eq1* and *JP-eq2*. *JP-eq1* presented an exaggerated situation where the toe inlet was relatively larger than the other inlets than *JP-eq2*. Vicente et al. (2002) attributed an increased flow rate from the toe at initial times to the larger reservoir volume available to the toe. Also, in their case, the toe inlet was not blocked and was assumed to produce flow. Based on the current simulation and its analysis, it is suggested that the higher flow rate from the toe was due to the increased inflow and the pressure drop available to it. The absence of blocking effect allowed for a higher pressure differential between the toe and the heel. Hence the instantaneous flow rate was not determined directly by the reservoir volume but by the pressure.

It would be appropriate to compare the performance of these jet pump type configuration against that of circumferential inlets. This is done in Figure 4.16 that compares the individual flow rate contribution and cumulative flow rate between the cases. It was observed that between *case-2* and *JP-eq2* the flow was more equalized from all inlets in the former. But higher contribution from inlet 1 and 5 was observed. The cumulative flow rate was higher for *case-2*. Cases *JP-incr* and *case-3* are also compared. Both had similar cumulative production profiles but there was slight advantage that was observed from the toe-inlet for *JP-incr*.

This analysis showed that initially at high equal pressures on the inlets at the start of production a high flow rate could be achieved from the toe-end stages by having larger inlets on them. The relative sizes can be selected as per the inlet pressure and pressure drop between the inlets. *JP-eq1* produced the most flow from the toe and *JP-eq2* produced the highest total flow rate. But in many situations, this might not be the requirement, as indicated by Dore Fernandes et al. (2006). For the purposes of mitigating water breakthrough into the well, flow rate equalization is desired and this



(a) Flow rate contribution



(b) Cumulative flow rate

Figure 4.16: Comparison of jet pump cases (dotted lines) with circumferential inlet cases (solid lines) from Table 4.1.

can be accomplished by using an inflow control device (ICD) as shown by Birchenko et al. (2010), Oyeka et al. (2014) and others.

The initial flow regime of the system can be quite different from the regime at a later production time when the inlet pressures are not all equal. All the studies mentioned above and in Chapter 2 show the flow rate result of ICD application at a certain time in the production life of a well. Although most publications showed

increase in total production over a certain time period, knowing the inevitability of decrease in reservoir pressure the suitability of the same ICD setup or perforation distribution might not be optimum. This decreasing pressure translated to a boundary condition for our simulations. This requires a time-dependent study of flow through the jet-pump configuration to assess the suitability of the present design. This study was undertaken and results presented in the next section.

4.4.2. Time-dependence of flow regimes

Figure 4.17 shows flow regimes and drained volume at different times for the annular jet pump cases. For case *JP-eq1* the flow regime was initially near *trickle* flow at $t = 20s$, with the fifth inlet dominating the total flow rate. This inlet also produced the most flow (Fig.4.17b) for the entire duration of the simulated time period with a total drainage of about 50% of the initial volume. The fifth inlet did not have any jet-pump configuration on it and there was no blocking effect on it from the downstream ones. Only the fifth inlet produced more than 50% of the initial volume. The other four inlets contributed to the total production as per the pressure gradient available to them.

For *JP-eq2* case the slightly larger inlet size $0.2w$ resulted in some *blocking* effect, observed from Figure 4.17c and 4.17d. The first inlet dominated for the simulated time period. The third and the fourth inlet produced less than the fifth inlet for the entire time. Again, the relatively large size of the fifth inlet allowed it to contribute more to the total flow rate and the other inlets were limited by their inlet sizes. At $t = 80s$ inlet 1 had drained the most ($\approx 60\%$) among all inlets while the fourth inlet had only drained $\approx 30\%$ of its initial volume.

Figure 4.17f corresponds to the incremental inlet size case *JP-incr*. For this case, the relative contribution to the total flow rate from all the inlets was about the same throughout the simulated time period. This suggests *trickle* flow regime for the entire duration. The shape of the regime curves remained similar at all times. This resulted

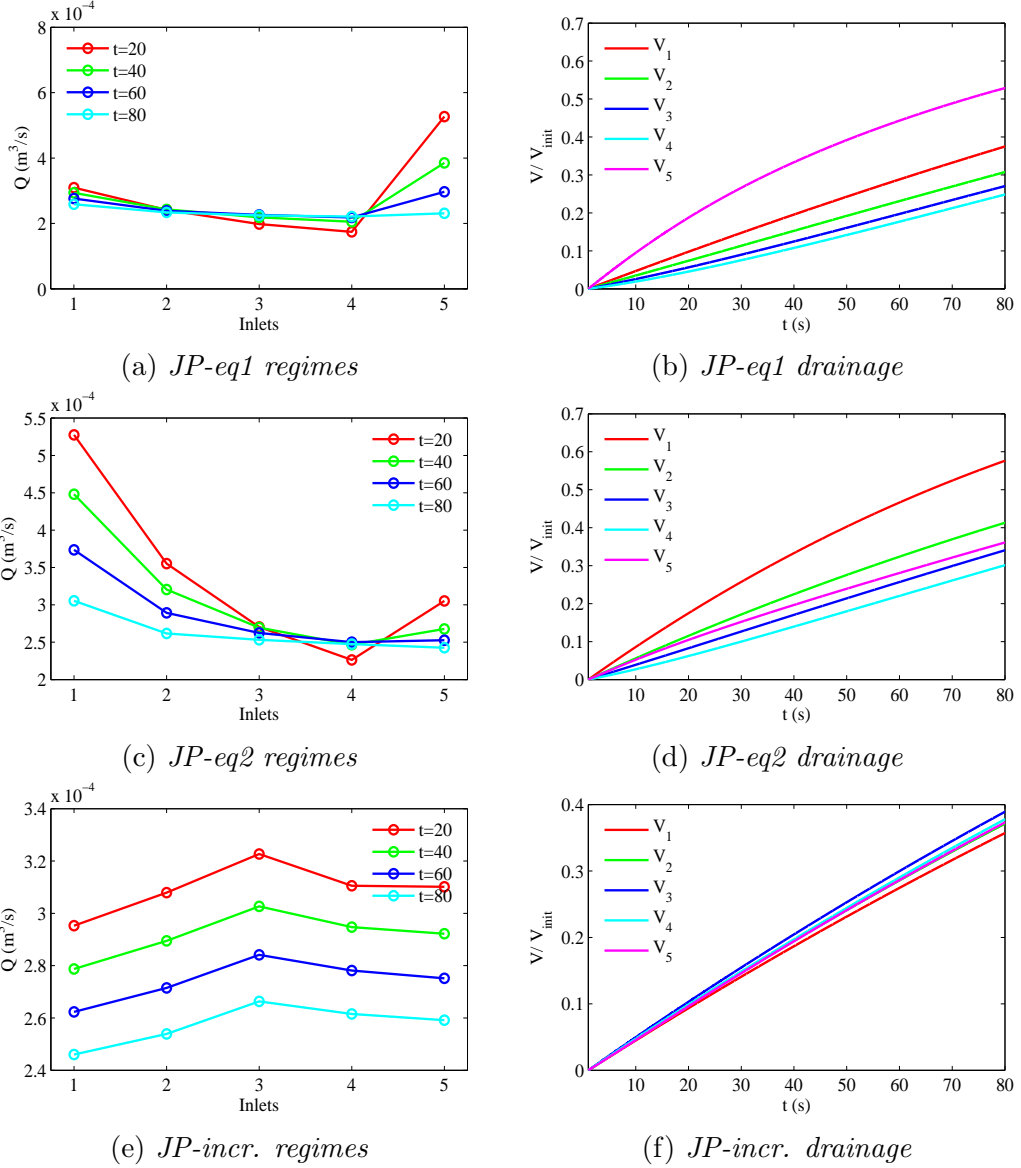


Figure 4.17: Flow regimes and volume drained over time for cases with annular jet pump inlets.

in nearly equal drainage from all inlets. This case suggests a desirable configuration where the segments of the reservoir associated with each inlet produce equal flow throughout the production period.

Figure 4.18 shows the volume drained from each inlet as a fraction of the initial volume V_{init} and also the total volume at the end of simulated time period, $t = 80$ s. As discussed earlier, for *JP-eq1* the fifth inlet was the most drained due to very little

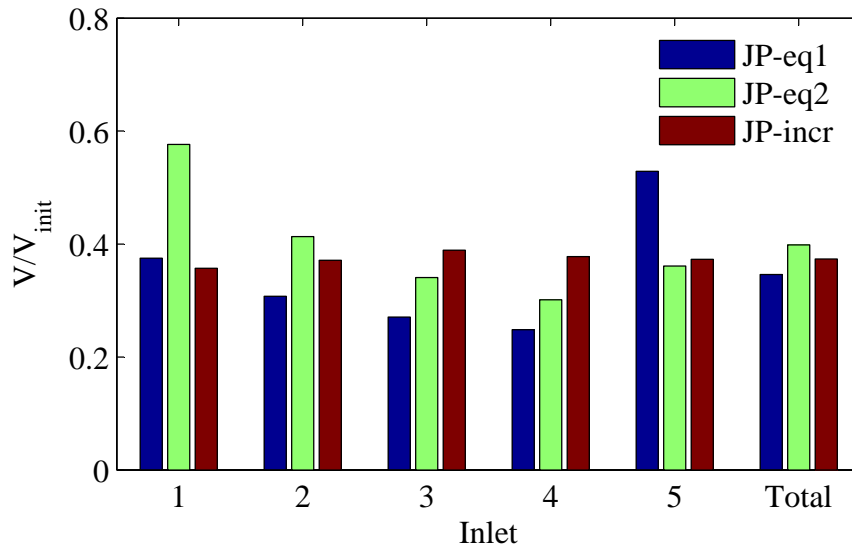


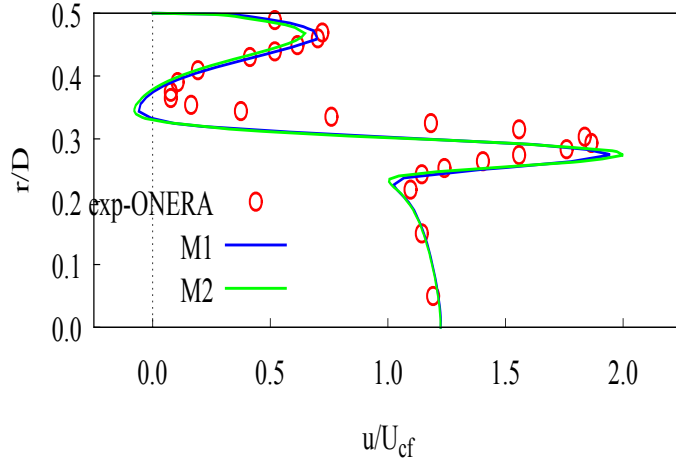
Figure 4.18: Volume drained for three cases with nozzles on inlets at $t=80s$.

blocking effect on it. The four downstream inlets had small sizes and hence lower flow rates associated with them for the simulated period. For *JP-eq2* the first volume was drained the most. That contributed to this case having maximum total production at the end. The third and fourth inlet produced less than the fifth inlet and were partially blocked. *JP-incr* was able to achieve a near homogeneous production profile. This case showed little sign of blocking at the beginning. The nozzle sizes on the jet-pump configurations were such that the inter-zone pressure drop was overcome by the inlet pressure and each inlet could contribute equal flow rate. Hence, the drainage from each inlet at the end was nearly equal. Such an arrangement of nozzle sizes would potentially benefit in draining more even volumes from the reservoirs associated with each perforation stage while maintaining a homogeneous flow regime from the well.

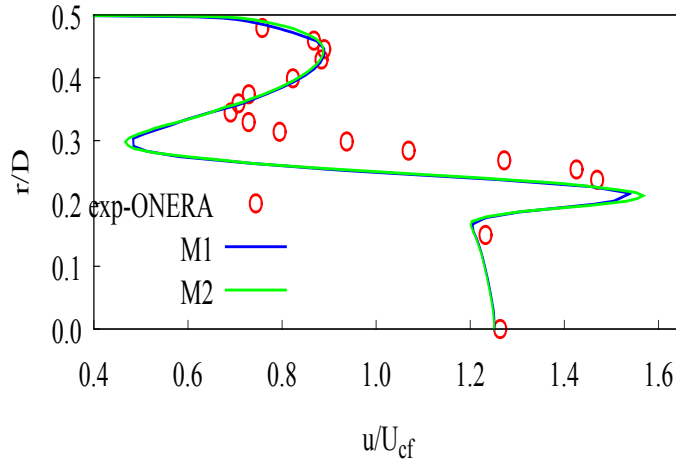
4.5. Annular inlet with discrete holes

4.5.1. Code Validation

As mentioned in Chapter 2 the geometry of a perforated inlet zone in a wellbore resembles a pre-burner (combustor) of staged combustion rocket engines. The main



(a) $x/d_j = 2$



(b) $x/d_j = 5$

Figure 4.19: Comparison of axial velocity for combustor geometry crossflow at different axial locations.

pipe of the combustor is like the wellbore and the jet inlets resembles the perforations on the pipe wall. The density of these perforations differs for every well. In the combustor case considered here there were eight jets in cross flow (JICF) spaced evenly around the circumference of the main pipe.

This configuration was studied using a three-dimensional domain and the details of the domain were presented in Chapter 3. Prière et al. (2005) conducted experimental and numerical studies (LES) on the combustor. The present simulation setup was first validated using those experimental results. As in the simulations, a 45° section

of the main pipe was considered as the domain with symmetry boundary conditions as described in Chapter 3. Two mesh resolutions were tested for obtaining a mesh independent solution. Mesh 1 had $\approx 4 \times 10^5$ elements while Mesh 2 had $\approx 1 \times 10^6$ elements. The flow Reynolds number based on the crossflow bulk velocity V_{cf} and the main pipe diameter D was 1.68×10^5 . The jet Re based on the jet diameter d_j and the jet average velocity V_j was 41×10^3 . The jet to crossflow momentum ratio J was 16. This is given as

$$J = \frac{\rho_{jet} U_j^2}{\rho_{cf} U_{cf}^2}. \quad (4.2)$$

As the densities of the two streams were equal, the jet to crossflow velocity ratio $r = U_j/U_{cf} = 4$. The mean field of the mixing region can be described by the velocity distribution. Figure 4.19 shows mean streamwise velocity profiles at two downstream locations, $2d_j$ and $5d_j$, from the injection point for steady state simulations. The shapes of the experimental and simulated velocity profiles are in reasonable agreement. The main flow features are captured by the $k - \epsilon$ turbulence model that was used in the present simulations, although slightly better prediction was obtained from LES simulations carried out by Prière et al. (2005). Also, no significant differences were observed between the two mesh resolutions tested here. This proved that the code turbulence model could be used at such high value of Re and, hence, also at lower values.

Friction factor for flow across the inlet zone is compared with experimental results of Jiang et al. (2001) in Figure 4.20. They conducted experiments using different perforation distributions on a pipe resembling a wellbore completion stage. They showed that pressure drop across a stage is dependent on parameters such as density of perforations (ϕ , holes per foot), azimuthal phasing (α), Reynolds number (Re) and ratio of perforation to main flow rate ($q_{in} \bar{Q}$). Based on these parameters they gave

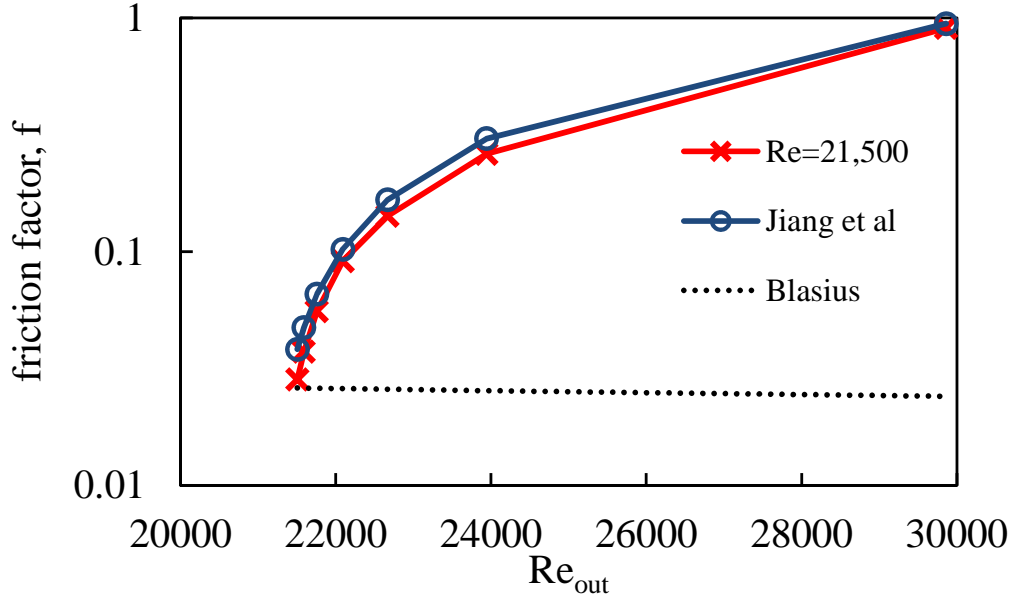


Figure 4.20: Comparison of friction factor across the jet with Jiang et al. (2001)'s experiments.

correlations of the form

$$f = aRe^b + C_n 2d\phi \frac{q_{in}}{Q}, \quad (4.3)$$

where a , b and C_n are constants obtained from analysis of the experimental data set. For the present simulations, the total inflow rate from the jets was taken to be eight times the inflow from one jet. For the purpose of comparison, one data set of Jiang et al. (2001) was chosen, with the parameters as follows: $\alpha = 90^\circ$, $\phi = 5$, $a = 0.873$, $b = -0.341$, $C_n = 2.344$.

The crossflow was kept constant at $Re_{cf} = 21,500$ and the jet velocity was varied for every simulation. This trend of increase in f was observed from the data sets presented by Jiang et al. (2001) but was not discussed. With increase in the jet velocity, the total flow rate at the outlet increased resulting in increased Re_{out} . The f values are in good agreement with the experimental results and the trend is also matched.

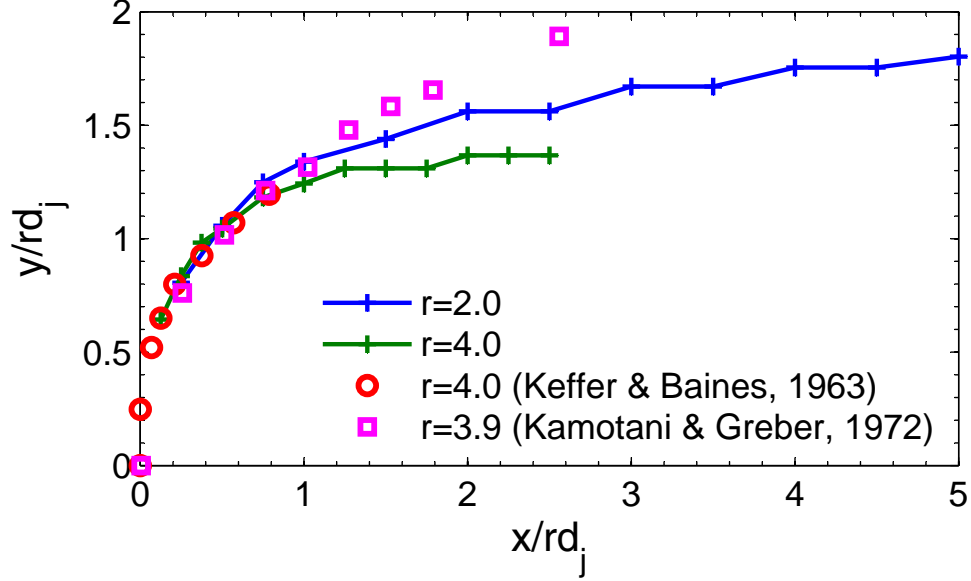


Figure 4.21: Comparison of jet trajectories for two different velocity ratios with published data. Here r is velocity ratio. Experimental data from Keffer and Baines (1963) & Kamotani and Greber (1972).

This gives confidence in the ability of the $k - \epsilon$ turbulence models in such a flow configuration and simulated Re . Further validation of the code was carried out using a single inlet in a crossflow and compared with results of Yuan et al. (1997). This study is presented in Appendix B for reference.

For the purpose of wellbore flow a lower Re flow was simulated. The crossflow Reynolds number Re_{cf} value was chosen as 5800 and the jet Reynolds number Re_j was varied for different steady state simulations. A velocity profile obtained from 1/7th power law for pipe flow was used as the inlet boundary condition so that when the crossflow interacts with the jet flow, the velocity profile is close to fully-developed. For the jet, a constant velocity across the inlet boundary was used.

Figure 4.21 shows comparison between simulated cases for $r = 2.0$ & 4.0 and published experimental data. It should be noted that the experimental data is for the canonical JICF experiments with the jet issuing in a two dimensional boundary layer. No such data was available for the Re that was simulated here. The commonly used ‘rd’ scaling has been employed (Mahesh (2013)). It can be observed that near

the jet injection point the trajectories matched with experimental data. Away from the jet injection, there was reasonable agreement but the penetration of the jet into the crossflow is not as high as the free crossflow cases of the experimental works. The jet penetration is lower than that for free crossflow case due to the geometry in consideration here. This is a major difference between the jet in the present case and the canonical JICF setting. Until now, only a handful of published works are available on the study of jets issuing in pipe flow and their interaction. More work is required to understand the mixing characteristics of the jet in a pipe cross flow.

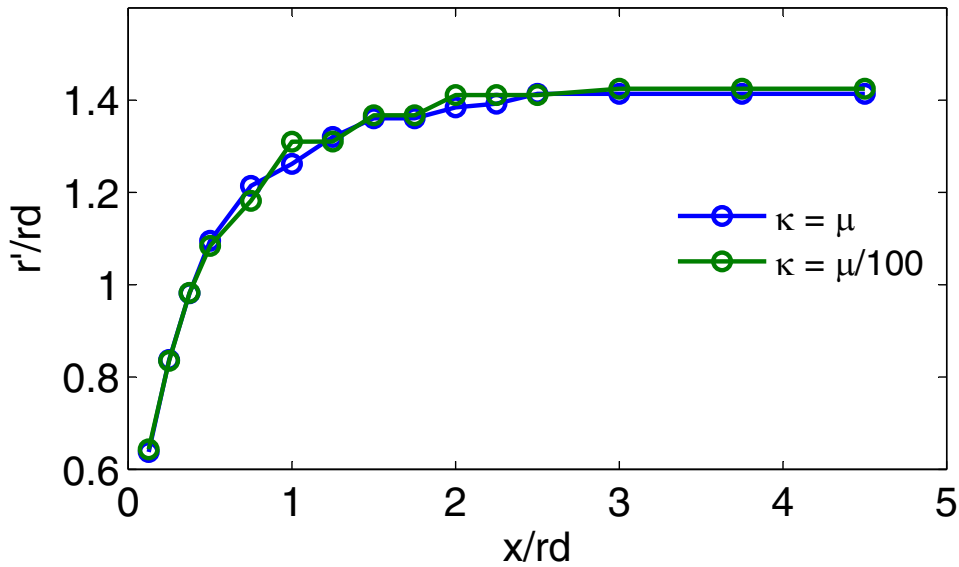


Figure 4.22: Comparison of jet trajectories for two different values of scalar diffusivity.

For the present simulations a passive scalar was introduced from the jet inlet. This scalar was tracked by solving equation 3.3. The scalar diffusivity κ was set equal to the fluid viscosity. The sensitivity of scalar diffusivity on the flow was studied by changing the value of κ . The result is shown in Figure 4.22 which compares the jet trajectory for $\kappa = \mu$ and $\kappa = 0.01\mu$. The two curves are identical very close to the jet exit. Away from the exit, some differences can be noticed, but not significant enough. Hence for all the simulations in this section $\kappa = \mu$ was used.

Using the above mentioned setup simulations were carried out for four different

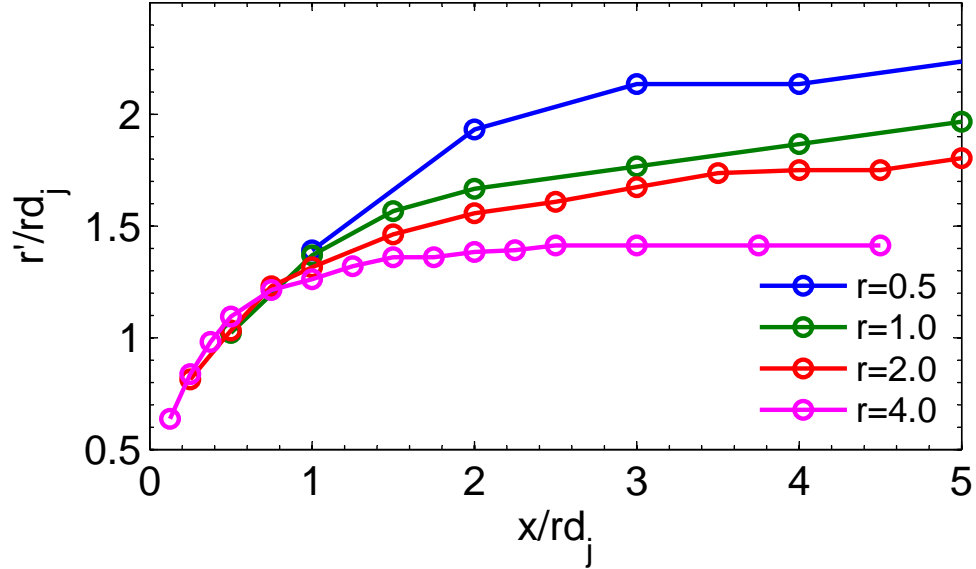


Figure 4.23: Comparison of jet trajectories for different velocity ratios.

velocity ratios. Mesh 2 was used for all the results presented here. Jet trajectories for these simulations are compared in Fig. 4.23. Once again, the rd scaling has been used. The trajectories were based on the maximum scalar concentration of the jet flow at downstream locations of the jet. It can be observed that the trajectories do not collapse using the rd scaling, especially as the distance from the jet injection point increases. This suggests that rd scaling might not be appropriate for jets injected into a confined crossflow (JICC) as in this case.

4.5.2. Mean flow

The various simulated velocity ratios presented an interesting study. With increase in velocity ratio, the flow from the jet had more momentum to penetrate the crossflow. This is observed from Figure 4.24 which presents non-dimensional mean axial velocity. The crossflow velocity profile changed downstream of the injection point with increasing velocity ratio. For low velocity ratios $r = 0.5$ and 1.0 , the cross-flow velocity profile did not change significantly. The velocity profiles became more parabolic shaped at further downstream locations, deviating away from the turbulent pipe flow profile of the crossflow. The penetration can be seen near the pipe

wall ($y/D = 0.5$) for the profiles. For $r = 2.0$ and 4.0 the velocity profile showed penetration of the jet at $x/d_j = 2$. Moving away from the injection point the sharp gradients in velocity diffused.

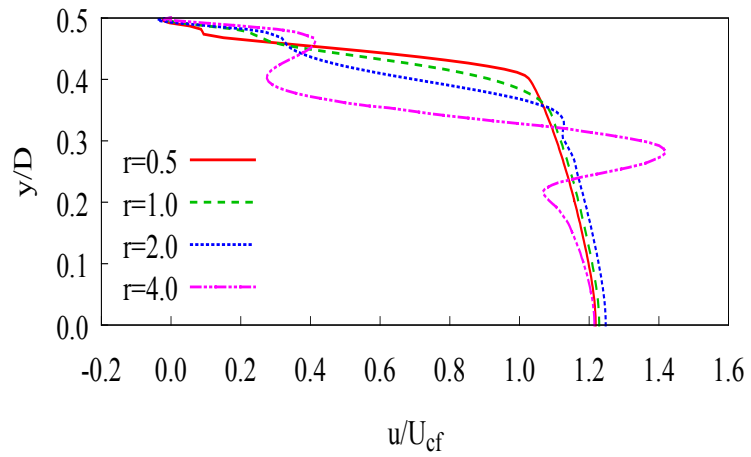
Figure 4.25 shows the mean velocity field near the jet exit. Figure 4.25a shows the stream-wise velocity normalized using the crossflow velocity V_{cf} . One can observe the regions of low and high velocities on the windward and leeward sides of the jet. These sides correspond to the two humps in the stream-wise velocity profiles shown in Figure 4.24, the leeward side near the pipe wall and the windward hump towards the center of the pipe. There is a region of recirculation very close to the jet exit, which effects the pressure drop characteristics of the crossflow.

Figure 4.25b shows the scalar field near the jet exit. The scalar showed the jet trajectory very clearly as it moved with the jet fluid; the crossflow had zero scalar concentration. The diffusion of the scalar can also be observed as a result of the scalar diffusivity being non-zero in Equation 3.3. Figures 4.25c and 4.25d show contours of normalized stream-wise velocity and stream-wise vorticity in a plane that is normal to the stream-wise direction located at $x = 2d_j$ downstream of the jet inlet. Using the symmetry planes of the domain all eight jets issuing into the crossflow present a pattern, similar to those obtained by Prière et al. (2005). The vorticity contours show the counter-rotating vortex pair that was formed downstream of the jet.

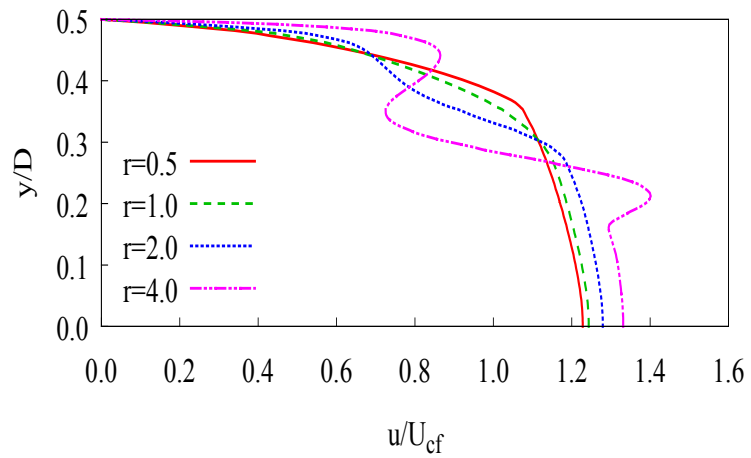
4.6. Annular jet pump - three-dimensional simulations

A three-dimensional nozzle geometry was used for the simulations described in this section. The overall picture of the jet pump nozzle on a inlet zone was obtained from 2D simulations described in section 4.4. Symmetry boundary conditions were used as described in Chapter 3.

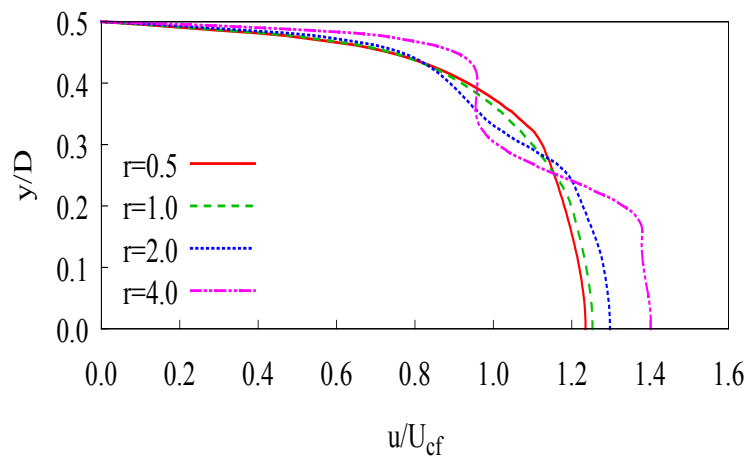
The main objective of an Inflow Control Device (ICD) is to control and homogenize the flow rate from all stages in a well to, ultimately, improve productivity and prevent



(a) $x/d_j = 2$



(b) $x/d_j = 5$



(c) $x/d_j = 10$

Figure 4.24: Comparison of axial velocity for combustor geometry crossflow at different axial locations.

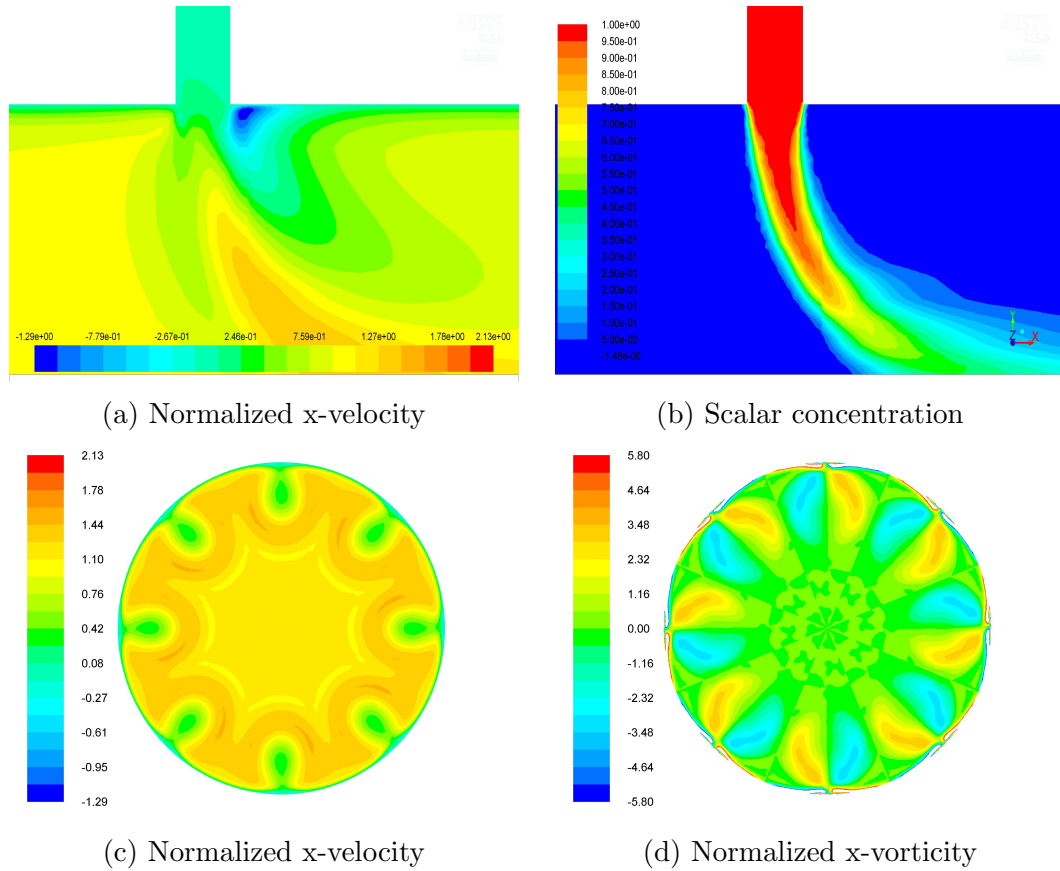


Figure 4.25: Contours of various quantities of the flow in the mixing region

early water breakthrough (Halvorsen et al. (2013), Birchenko et al. (2010), etc.). The present nozzle configuration can serve as an ICD by controlling the flow rate. This was shown using two-dimensional simulations in section 4.4. For incompressible flow considered in this work, the nozzle opening size determines the flow rate along with pressure at the inlet. The ICD could be designed to minimize the energy losses in the flow. The converging section, diverging section and the throat design depend on the operating flow rate (Re). Various studies like Shimizu et al. (1987), Elger et al. (1994), Xiao et al. (2013), etc. present designs of annular jet-pumps that could be modified to fit the present application in horizontal wellbores.

A mesh resolution test was carried out for the 3D domain of nozzle on the circumferential inlet as described Chapter 3. Mesh 1 contained 1.5×10^5 volume elements and Mesh 2 contained 1.0×10^6 elements. Structured grid was used for both mesh

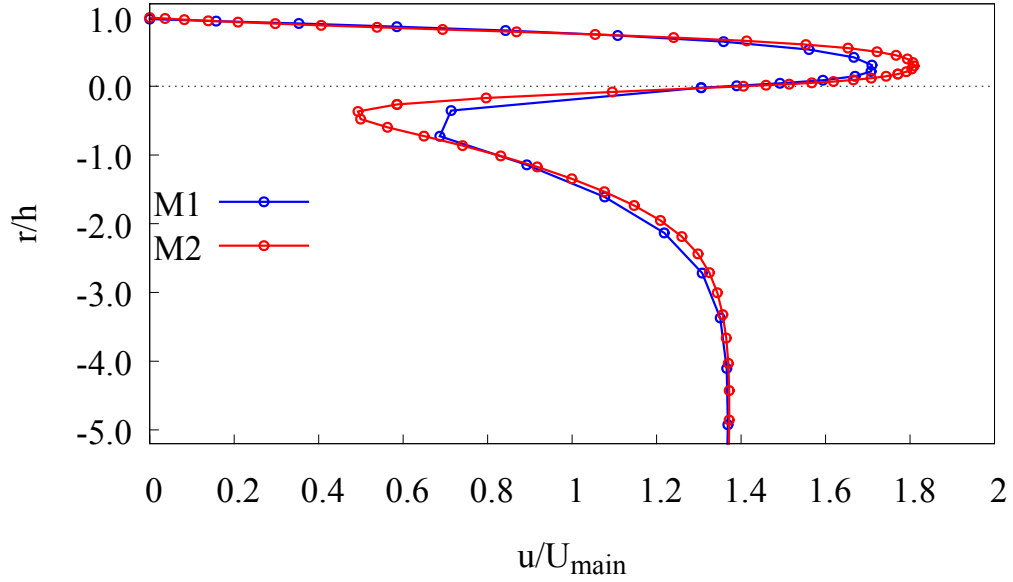
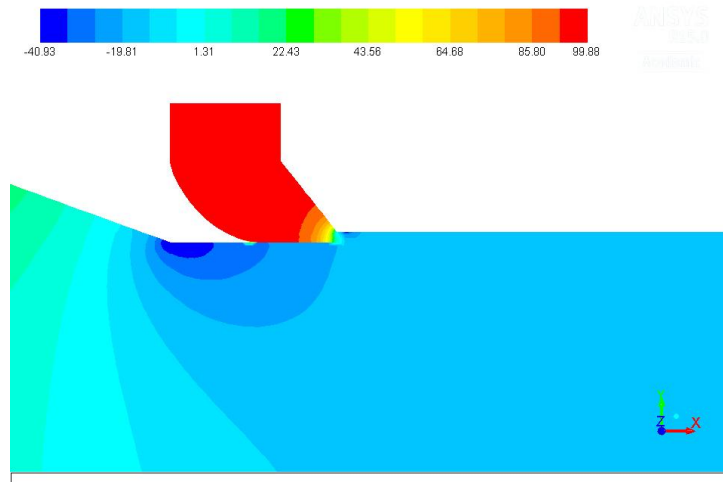


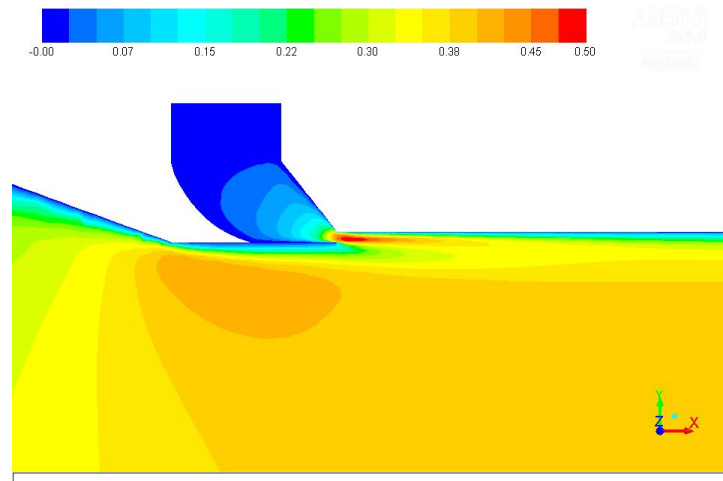
Figure 4.26: Axial velocity profile comparison for mesh resolution test of 3D simulation at $x=2h$ downstream of the nozzle. $k-\epsilon$ model was used for turbulence modeling

resolutions. Mesh 1 contained 15 mesh points across the nozzle exit and Mesh 2 contained 25 points. The $k-\epsilon$ model was used for turbulence modeling. Total pressure boundary conditions were imposed on the crossflow inlet and the circumferential inlet and a static pressure on the outlet boundary. Figure 4.26 shows velocity profiles for the two mesh resolutions at $x = 2h$, where h is the nozzle width. The crossflow Reynolds number Re_{cf} was 13,300. For Mesh 1, $y^+ = 0.7$ near the outlet and for Mesh 2, $y^+ = 0.2$. The maximum velocity from the nozzle differs for the two mesh resolutions, as does the velocity near the nozzle wall separation at $r/h = 0$. Here, r is the radial distance from the nozzle separator, positive values indicate position towards pipe wall and negative values toward pipe axis. For these simulations, a pressure boundary condition was used for the crossflow inlet as well as the circumferential inlet.

Figures 4.27a and 4.27b show pressure and stream-wise velocity contours near the nozzle on center plane with z -direction normal. This illustrates the utility of the nozzle injector where the inlet pressure is converted to dynamic pressure only near the



(a) Static pressure



(b) Stream-wise velocity

Figure 4.27: Pressure and x-velocity contours on center plane for 3D simulation of inlet with nozzle.

nozzle. This depends on the opening size and design of the nozzle. To reduce losses and avoid any recirculation, the nozzle was provided with a circular shaped entrance leading upto the separator wall. The nozzle opening is such that flow from it enters the main flow pipe almost parallel to the crossflow. This is evident from Figure 4.28a which shows the velocity profile at a distance of $1h$ downstream of the nozzle location, where h is the nozzle opening width. The zero line corresponds to location of the separation wall between nozzle and main flow stream. Two turbulence models were used in these simulations - the $k - \epsilon$ and $k - \omega$ -Shear Stress Transport model (Menter

(1994))- to observe any major differences in the flow features predicted by the two models. Both models predicted similar trends in velocity distribution. There was some difference between the two in prediction of velocity profile near $r/h = -0.5$. This is the zone where the two streams with different velocities (shear layer) mix together and momentum transfer takes place.

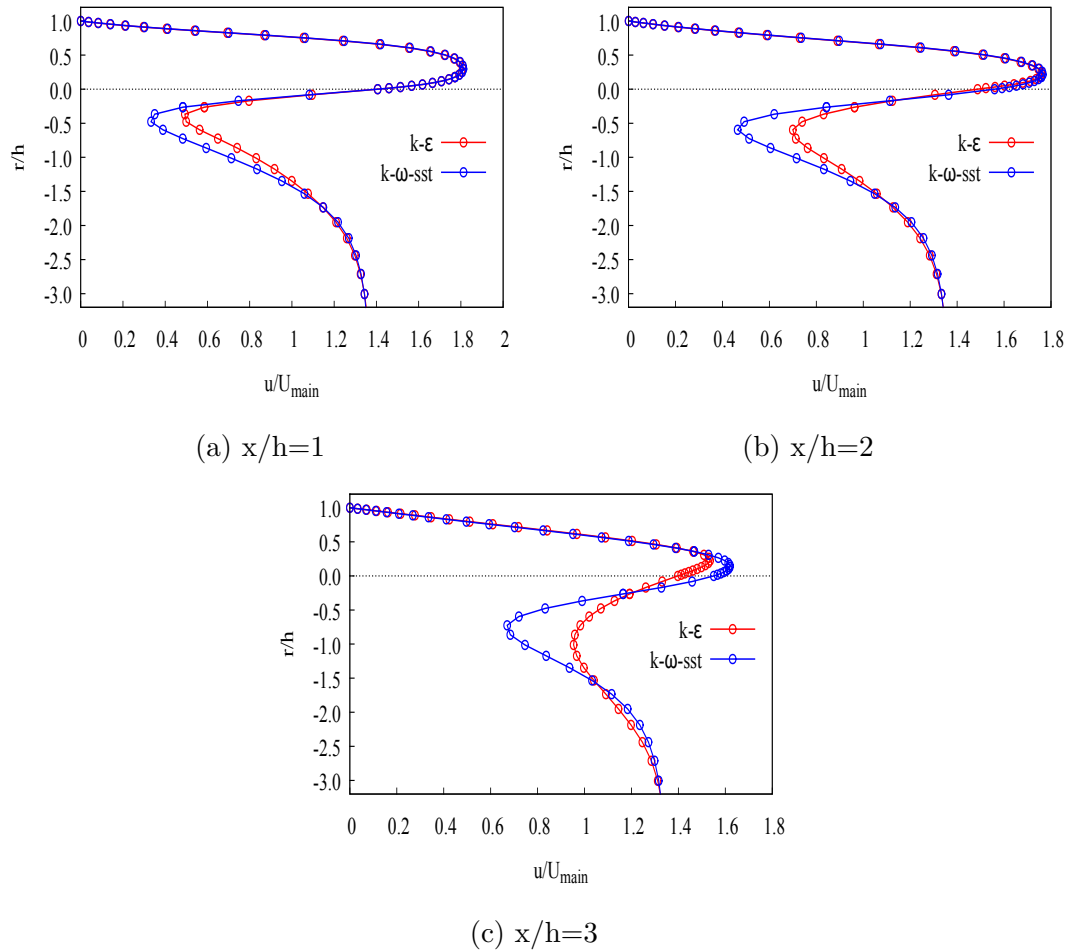


Figure 4.28: Axial velocity profiles downstream of the jet injection plane, from 3D simulation of a jet pump.

The flow from the nozzle presents an advantage over flow directly from a circumferential inlet or discrete perforations into the crossflow. The pressure drop due to mixing of the two fluid streams would be higher for the perforations than the nozzle. This is due to the direction of the jet flow being normal to the crossflow and the losses

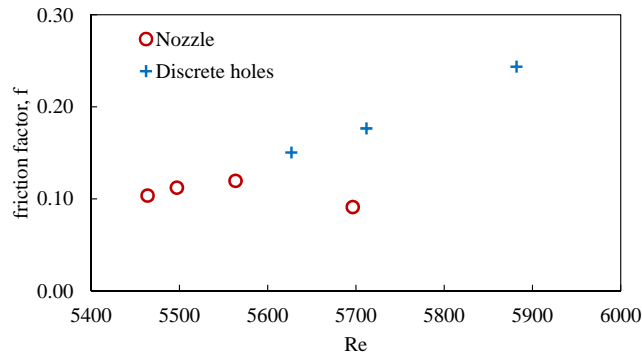


Figure 4.29: Friction factor comparison between discrete holes and nozzle

associated with the turbulent mixing of the two streams. Figure 4.29 compares the frictional pressure drop across the nozzle and the combustor geometry with discrete holes. In these steady state simulations, the crossflow Reynolds number Re_{cf} was held constant at 5430 for the nozzle case and 5540 for the combustor case. An inflow velocity profile was prescribed using the one-seventh power law to aid the development of a fully developed flow before mixing of the injection. The injection stream in case of combustor or the annular inlet in case of nozzle were specified a constant velocity inlet condition. Hence, each point on the plot represents a different injection velocity for the same crossflow conditions. It can be observed that the friction factor is slightly lower for the nozzle cases than the combustor cases (discrete holes). This suggests a greater loss due to mixing of two streams with the injection stream perpendicular to the crossflow when compared with nozzle cases. The nozzle design also has losses associated with it. A better design will potentially further decrease the energy losses and help to enhance production.

The three-dimensional simulations give details of the flow field that could not be obtained from 2D simulations. The design of the nozzle and other parts of the jet-pump configuration can be studied numerically using 3D flow simulations and improved further to suit different Re and applications such as wells with predominantly gas flow. The circumferential inlet can also be replaced by discrete perforation holes

to study flow interaction among them and its effect on the overall crossflow. Although RANS turbulence models have found to be unable to predict JICF in great detail (Colletti et al. (2013), Jessen et al. (2007)), the basic flow features can still be observed. Their use in engineering flow problems due to lower computational requirements and complex flow geometries is common.

5. Conclusions

CFD simulation of a wellbore with multiple stages was performed using an axisymmetric pipe geometry with five annular inlets. This was a simplified inlet used in place of perforation zones that are created in an actual wells. Flow near these inlet zones was simulated while flow away from the zone was modeled using a pressure drop model. Thus with a relatively small computational domain, a wellbore with as much as $105m$ between each of the five inlet zone was modeled and simulations were carried out.

In a system with multiple stages, for a given pressure and inlet size, three different flow regimes were observed - *trickle*, *partially blocked* and *blocked flow* regime. In trickle flow, the inlets functioned independently of each other. There was minimal limiting effect on the upstream inlets due to the downstream ones. In a partially blocked flow regime, the inlets near the heel dominated while the fully blocked regime was characterized by near maximum flow rate from the first inlet near the heel (outlet). The inlets downstream of the first inlet were blocked. The well known heel-toe effect would fall under this classification.

It was observed that with increase in inlet size, the total flow rate for the wellbore also increased and the flow regime changed. Increasing the inlet size shifted the regime from trickle flow towards fully blocked flow. Within the limits studied here, increase in pressure for constant inlet size increased total and individual production, but the flow regime did not change. It is clear that regime change can occur over a wider range of pressure variation.

A simple reservoir model was used to study the effect of dynamic change in pressure on the behavior of individual inlets in a multi-inlet setting. The equilibration time scale T_e and reservoir depletion time scale T_d were identified. A lumped parameter type pressure drop model was used to account for pressure loss between the

inlets along the pipe axis. Coupling this with the CFD simulation of flow near the inlets showed how the individual inlets interacted dynamically. The change in regime with depleting reservoirs was compared to the actual field data from Fig. 1.2 which has 31 stages. The results also indicated the existence of a blocking type effect that was observed in the work of Vicente et al. (2002, 2004), which changes with pressure draw-down and time. It was concluded that the actual well shifted from a partially flow limited regime at the 30-day mark towards a trickle flow regime at the 155-day mark. The effect of inlet size on initial production and over time was investigated and compared.

Large, small and variable inlet sizes were used on the inflow zones. For the variable case, the inlet sizes increased starting from the heel and increasing towards the toe to achieve homogeneous production profile. The total flow rate over time and fraction of initial volume drained was compared for the three cases. The small inlet case performed better than the other two cases in draining the maximum volume. The initial production profile would change over time and this effect needs to be included in designing any well.

Simulations were also carried out on a three-dimensional grid for flow in a combustor geometry, resembling a perforation zone in horizontal wells. The flow features were reasonably duplicated for high Re from Prière et al. (2005). Simulations were conducted for lower Re flows applicable to wells with significant liquid production. General friction factor trend agreement was achieved for such flows on comparison with experimental work of Jiang et al. (2001).

Taking this analysis further, a nozzle was designed based on available designs of annular jet pumps in the literature and this was constructed around a perforation zone. Two-dimensional simulations were carried out with nozzles located near four inlets; the fifth inlet near the toe was allowed to flow freely into the wellbore. The proposed design could be used as an inflow control device to modify the production

profile of the well. Three dimensional simulations of the design were also carried out using symmetry planes and comparisons were made with a combustor geometry with discrete holes.

In conclusion, the present study is a novel attempt at understanding flow dynamics in a multiple stage horizontal wellbore. The specific flow regimes that apply to any given well will depend on the well diameter, inlet sizes and spacing, production flow rates, reservoir and well bore pressures, and the fluids involved. Coupling such simulations with reservoir models can provide more information about time-scales and dynamics of a specific well. But important aspects of the fluid dynamical interaction between stages can be investigated independently of specific reservoir model coupling. The present study makes a case for management of completions in a horizontal wellbore, based on more accurate determination of the flow states in the well.

6. Future work

CFD simulations can be used to assess various new designs of inflow control devices, including jet-pump-like configurations, in the oil production process. To better understand flow in these devices and come up with efficient designs more accurate simulations are required.

The effect of the design of nozzle / jet-pump was not considered in the present work. That will be explored further for predicting the efficiency of the jet pump under time varying conditions.

The presence of discrete inlets on flow thorough the jet-pump / nozzle configuration is also to be studied in future. The pressure loss in the nozzle due to flow from these inlets is important and further simulations need to be carried out to analyze this issue.

Multiphase flow is a common occurrence in oil and gas wells. Further studies need to be undertaken to determine the suitability of an enhanced version of present hybrid method in such cases.

Under high pressure and flow rates, compressible flow is predicted to occur in these wells. The flow behavior can potentially be very different under varying density and/or high velocities such as in wells primarily producing natural gas.

References

- Aadnoy, B. and Hareland, G. (2009). Analysis of Inflow Control Devices. *Offshore Europe*, (September):8–11.
- Agrawal, S. S., Gregory, G. A., and Govier, G. W. (1973). An Analysis of Horizontal Stratified Two-phase Flow in Pipes. *The Canadian Journal of Chemical Engineering*, 51(3):280–286.
- Ali, M. S. (2003). *Mixing of a Non-Buoyant Turbulent Jet Group in Crossflow*. Master's thesis, The Univ. of Hong Kong, Hong Kong.
- American-Petroleum-Institute (2014). Hydraulic Fracturing Primer. Technical report, American Petroleum Institute, Washington, DC.
- ANSYS (2014). ANSYS Fluent, Release 15.0, User Guide.
- Asheim, H., Kolnes, J., and Oudeman, P. (1992). A Flow Resistance Correlation for Completed Wellbore. *Journal of Petroleum Science and Engineering*, 8(2):97–104.
- Birchenko, V., Muradov, K., and Davies, D. (2010). Reduction of the Horizontal Well's HeelToe Effect with Inflow Control Devices. *Journal of Petroleum Science and Engineering*, 75(1-2):244–250.
- Cambonie, T., Gautier, N., and Aider, J.-L. (2013). Experimental Study of Counter-Rotating Vortex Pair Trajectories Induced by a Round Jet in Cross-Flow at Low Velocity Ratios. *Experiments in Fluids*, 54(3):1475.
- Coletti, F., Benson, M., Ling, J., Elkins, C., and Eaton, J. (2013). Turbulent Transport in an Inclined Jet in Crossflow. *International Journal of Heat and Fluid Flow*, 43:149–160.

- Davoudzadeh, F., Forliti, D., Le, A.-T., and Vu, H. (2012). Numerical Simulation of Confined Multiple Transverse Jets. In *42nd AIAA Fluid Dynamics Conference and Exhibit*, Reston, Virginia. American Institute of Aeronautics and Astronautics.
- Dikken, B. J. (1990). Pressure Drop in Horizontal Wells and Its Effect on Production Performance. *Journal of Petroleum Technology*, 42(11):1426–1433.
- DOE/EIA (2014). Enhanced Oil Recovery (web page: <http://energy.gov/fe/science-innovation/oil-gas-research/enhanced-oil-recovery>).
- Dore Fernandes, P., Silva, M. G. F., and Bedrikovetsky, P. (2006). A New IOR Technology To Homogenize Horizontal Well Injectivity/Productivity Profile. In *SPE/DOE Symposium on Improved Oil Recovery*, number figure 3. Society of Petroleum Engineers.
- Elger, D. F., Taylor, S. J., and Liou, C. P. (1994). Recirculation in an Annular-Type Jet Pump. *Journal of Fluids Engineering*, 116(4):735.
- Ferziger, J. H. and Perić, M. (1996). *Computational Methods for Fluid Dynamics*. Springer Berlin, third edition.
- Fripp, M., Zhao, L., and Least, B. (2013). The Theory of a Fluidic Diode Autonomous Inflow Control Device. In *SPE Middle East Intelligent Energy Conference and Exhibition*, number October, pages 28–30. Society of Petroleum Engineers.
- Furui, K., Zhu, D., and Hill, A. (2005). A comprehensive model of horizontal well completion performance. *SPE Production & Facilities*, (August):207–220.
- Gosline, J. E. and O'Brien, M. P. (1934). The Water Jet Pump. In *University of California Publications in Engineering Vol 3 (3) 167-190*, pages 167–190. University of California Press, Berkeley.

- Goswick, R. A. and LaRue, J. L. (2014). Utilizing Oil Soluble Tracers to Understand Stimulation Efficiency Along the Lateral. In *SPE Annual Technical Conference and Exhibition*, pages 1–10. Society of Petroleum Engineers.
- Halvorsen, M., Elseth, G., and Naevdal, O. M. (2013). Increased Oil Production at Troll by Autonomous Inflow Control with RCP valves. In *SPE Annual Technical Conference and Exhibition*. Society of Petroleum Engineers.
- Hill, A. and Zhu, D. (2008). The Relative Importance of Wellbore Pressure Drop and Formation Damage in Horizontal Wells. *SPE Production & Operations*, 23(2):232–240.
- Hiller, J. (2014). Players in Eagle Ford Shale Work on Upping Their Games (News article in Houston Chronicle 17 Sep, 2014).
- Hirt, C. W. and Nichols, B. D. (1981). Volume of Fluid (VOF) Method for the Dynamics of Free Boundaries. *Journal of Computational Physics*, 39(1):201–225.
- Jessen, W., Schröder, W., and Klaas, M. (2007). Evolution of Jets Effusing from Inclined Holes into Crossflow. *International Journal of Heat and Fluid Flow*, 28(6):1312–1326.
- Jha, P. N. (2011). *Flow Interaction Between Multiple Cross-Flow Inlets in a Horizontal Pipe or Channel*. Master’s thesis, University of Houston.
- Jiang, W., Sarica, C., Ozkan, E., and Kelkar, M. (2001). Investigation of the Effects of Completion Geometry on Single-Phase Liquid Flow Behavior in Horizontal Wells. *Journal of Energy Resources Technology*, 123(2):119.
- Kamotani, Y. and Greber, I. (1972). Experiments on Confined Turbulent Jets in Cross-Flow. Technical report, NASA, Washington, DC.

- Karimi-Fard, M. and Durlofsky, L. (2011). An Expanded Well Model for Accurate Simulation of Well-Reservoir Interactions. *Proceedings of SPE Reservoir Simulation Symposium*.
- Keffer, J. and Baines, W. (1963). The Round Turbulent Jet in a Cross-Wind. *Journal of Fluid Mechanics*, (July).
- King, G. E. (2012). Hydraulic Fracturing 101: What Every Representative, Environmentalist, Regulator, Reporter, Investor, University Researcher, Neighbor and Engineer Should Know About Estimating Frac Risk and Improving Frac Performance in Unconventional Gas and Oil Wells. In *SPE Hydraulic Fracturing Technology Conference*, pages 1–80. Society of Petroleum Engineers.
- Lai, A. C. and Lee, J. H. (2010). Multiple Tandem Jet Interaction in a Crossflow. *Journal of Hydrodynamics, Ser. B*, 22(5):639–643.
- Long, X. P., Zeng, Q. L., Yang, X. L., and Xiao, L. (2012). Structure Optimization of an Annular Jet Pump Using Design of Experiment Method and CFD. *IOP Conference Series: Earth and Environmental Science*, 15(5):052020.
- Mahesh, K. (2013). The Interaction of Jets with Crossflow. *Annual Review of Fluid Mechanics*, 45(1):379–407.
- Marsalek, J. (1984). Head Losses at Sewer Junction Manholes. *Journal of Hydraulic Engineering*, 110(8):1150.
- Mathiesen, V., Werswick, B., Aakre, H., and Elseth, G. (2011). Autonomous Valve, A Game Changer Of Inflow Control In Horizontal Wells. In *Offshore Europe*. Society of Petroleum Engineers.
- Menter, F. R. (1994). Two-Equation Eddy-Viscosity Turbulence Models for Engineering Applications. *AIAA Journal*, 32(8):1598–1605.

- Ouyang, L. and Aziz, K. (2000). A Homogeneous Model for Gas-Liquid Flow in Horizontal Wells. *Journal of Petroleum Science and Engineering*, pages 119–128.
- Ouyang, L.-B., Arbabi, S., and Aziz, K. (1998). General Wellbore Flow Model for Horizontal, Vertical, and Slanted Well Completions. *SPE Journal*, 3(02):124–133.
- Oyeka, O., Felten, F., and Least, B. (2014). Screen-Inflow-Design Considerations with Inflow Control Devices in Heavy Oil. *SPE Heavy Oil Conference-Canada*.
- Penmatcha, V. and Aziz, K. (1999). Comprehensive Reservoir/Wellbore Model for Horizontal Wells. *SPE Journal*, 4(03):224–234.
- Prière, C., Gicquel, L., Gajan, P., and Strzelecki, A. (2005). Experimental and Numerical Studies of Dilution Systems for Low-Emission Combustors. *AIAA journal*, 43(8):1753–1766.
- Ragab, A., Brandstaetter, W., and Shalaby, S. (2008a). CFD Simulation of Multiphase Flows in Horizontal and Inclined Pipes. *Oil Gas-European Magazine*, 34(1):34–40.
- Ragab, A., Brandstaetter, W., and Shalaby, S. (2008b). Numerical Simulation of Slug Flow Phenomena in Horizontal and Inclined Pipelines. *Oil Gas-European Magazine*, 34(4):194–199.
- Ramamurthy, A. S. and Zhu, W. (1997). Combining Flows in 90 Junctions of Rectangular Closed Conduits. *Journal of Hydraulic Engineering*, 123(11):1012–1019.
- Sadr, R. and Klewicki, J. C. (2003). An Experimental Investigation of the Near-Field Flow Development in Coaxial Jets. *Physics of Fluids*, 15(5):1233.
- Shimizu, Y., Nakamura, S., Kuzuhara, S., and Kurata, S. (1987). Studies of the Configuration and Performance of Annular Type Jet Pumps. *Journal of Fluids Engineering*, 109(3):205.

- Su, Z. and Gudmundsson, J. (1998). Perforation Inflow Reduces Frictional Pressure Loss in Horizontal Wellbores. *Journal of Petroleum Science and Engineering*, 19(3-4):223–232.
- Taitel, Y. and Dukler, A. (1976). A Model for Predicting Flow Regime Transitions in Horizontal and Near Horizontal Gas-liquid Flow. *AIChE Journal*, 22(1):47–55.
- Tennekes, H. and Lumley, J. (1972). *A First Course in Turbulence*. MIT Press, Cambridge, MA, first edition.
- Vicente, R., Sarica, C., and Ertekin, T. (2002). A Numerical Model Coupling Reservoir and Horizontal Well-Flow Dynamics: Transient Behavior of Single-Phase Liquid and Gas Flow. *SPE Journal*, (March):6–8.
- Vicente, R., Sarica, C., and Ertekin, T. (2004). A Numerical Model Coupling Reservoir and Horizontal Well Flow Dynamics Applications in Well Completions, and Production Logging. *Journal of Energy Resources Technology*, 126(3):169.
- Winoto, S., Li, H., and Shah, D. (2000). Efficiency of Jet Pumps. *Journal of Hydraulic Engineering*, (February):150–156.
- Xiao, L., Long, X., Li, X., Zeng, Q., and Yang, X. (2013). Numerical Investigation on the Recirculation in Annular Jet Pumps. *Journal of Mechanical Science and Technology*, 27(6):1603–1609.
- Yalniz, M. and Ozkan, E. (2001). A Generalized Friction-Factor Correlation To Compute Pressure Drop in Horizontal Wells. *SPE Production & Facilities*, 16(4).
- Yu, D., Ali, M. S., and Lee, J. H. W. (2006). Multiple Tandem Jets in Cross-Flow. *Journal of Hydraulic Engineering*, 132(9):971.

- Yuan, H., Sarica, C., Miska, S., and Brill, J. P. (1997). An Experimental and Analytical Study of Single-Phase Liquid Flow in a Horizontal Well. *Journal of Energy Resources Technology*, 119(1):20.
- Zagarola, M. and Smits, a. (1997). Scaling of the Mean Velocity Profile for Turbulent Pipe Flow. *Physical Review Letters*, 78(2):239–242.
- Zhang, Q., Wang, Z., Wang, X., and Yang, J. (2014). A New Comprehensive Model for Predicting the Pressure Drop of Flow in the Horizontal Wellbore. *Journal of Energy Resources Technology*, 136(4):042904.
- Zhao, C.-H., Zhu, D. Z., and Rajaratnam, N. (2006). Experimental Study of Surcharged Flow at Combining Sewer Junctions. *Journal of Hydraulic Engineering*, 132(12):1259.
- Zitha, P., Felder, R., Zornes, D., Brown, K., and Mohanty, K. (2008). Increasing Hydrocarbon Recovery Factors.

Appendix

A. Governing equations for axisymmetric flow solution

Cylindrical coordinates are chosen to take advantage of symmetry and in axisymmetric flows the tangential velocity component vanishes ($u_\phi = 0$). The remaining quantities are independent of ϕ . For two-dimensional axisymmetric geometries having incompressible flow, the Navier-Stokes equation is given by

$$\rho \left(\frac{\partial u_r}{\partial t} + u_r \frac{\partial u_r}{\partial r} + u_z \frac{\partial u_r}{\partial z} \right) = -\frac{\partial p}{\partial r} + \mu \left[\frac{1}{r} \frac{\partial}{\partial r} \left(r \frac{\partial u_r}{\partial r} \right) + \frac{\partial^2 u_r}{\partial z^2} - \frac{u_r}{r^2} \right] + f_r, \quad (1)$$

$$\rho \left(\frac{\partial u_z}{\partial t} + u_r \frac{\partial u_z}{\partial r} + u_z \frac{\partial u_z}{\partial z} \right) = -\frac{\partial p}{\partial z} + \mu \left[\frac{1}{r} \frac{\partial}{\partial r} \left(r \frac{\partial u_z}{\partial r} \right) + \frac{\partial^2 u_z}{\partial z^2} \right] + f_z, \quad \text{and} \quad (2)$$

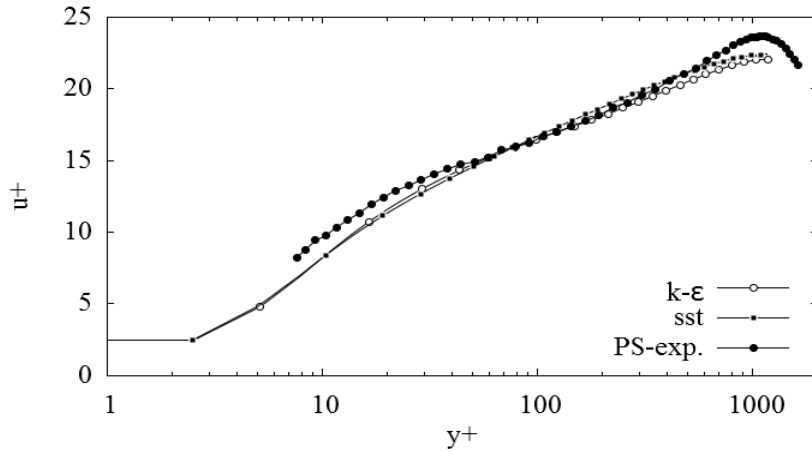
$$\frac{1}{r} \frac{\partial}{\partial r} (r u_r) + \frac{\partial u_z}{\partial z} = 0, \quad (3)$$

where z and r are the axial and radial directions respectively and f stands for body forces applicable on the fluid.

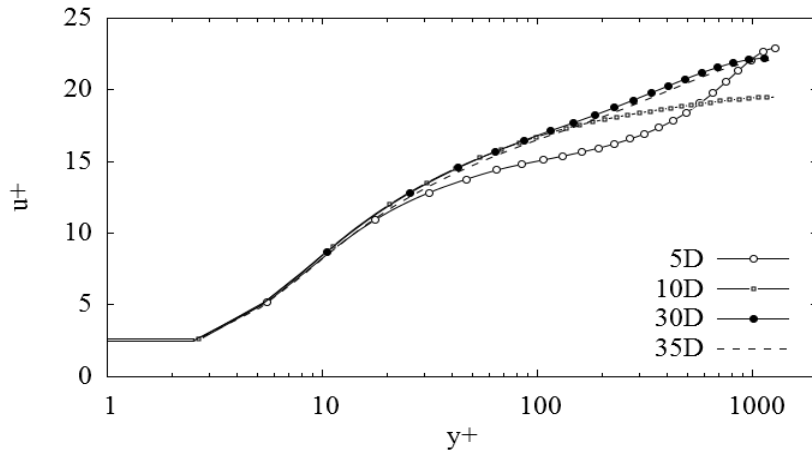
B. Turbulence Model and Development length

Figure A.1a shows comparison of two turbulence models for flow through the domain. Only I_5 was active and a flow rate was prescribed to this boundary such that the Re based on the average outflow velocity at the heel and pipe diameter was 43,845. Such a Re was chosen for comparison purposes. The figure gives a classic semi-log plot of non-dimensional velocity as a function of distance from the wall and results from $k-\epsilon$ (with enhanced wall treatment, $k-\epsilon$) and $k\omega$ -SST (SST) models are compared with experimental results of Zagarola and Smits (1997) that were obtained the Princeton Super-pipe database. The experimental result (PS-exp.) corresponds to $Re = 41,727$. The velocity profile compared here is at a location 35D downstream of the inlet when the velocity profile had developed. Both turbulence

models were in agreement with the experimental results. Hence, for the present computation, the $k - \epsilon$ model was chosen without loss of accuracy or physics of the flow features. The mesh was constant for all these cases. More details about the turbulence models can be found in ANSYS (2014). Here $y^+ (= yu_\tau/\nu)$, is the wall co-ordinate, made dimensionless with the friction velocity $u_\tau (= \sqrt{\tau_w/\rho})$, and $u^+ (= u/u_\tau)$ is the dimensionless velocity.



(a)



(b)

Figure A.1: (a) Comparison of turbulence models for a channel flow. (b) Determination of development length for turbulent cross-flow using *Case-1*. One side inlet (I_5) flowed into the domain, locations correspond to downstream from I_5 .

To ensure that the distance between two inlets was sufficient for fully developed

flow, simulations were performed with a single side inlet (I_5) with flow conditions chosen to give a Reynolds number of 43,845 at the outlet. Figure A.1b shows the velocity profiles at different locations downstream of the side-inlet.

There is convergence at a distance of 35D from the inlet, for the velocity profiles. To be conservative, the distance between two side-inlets was 40D in the channel simulations presented in this paper, which adequately allowed for flow development even at slightly higher Reynolds numbers. It should be noted that the Re goes to a high value near the heel of the pipe as it increases with cumulative flow rate from each inlet, starting from the toe. Hence, this inter-zone axial spacing of 40D was judged sufficient for fully developed flow.

C. Code Validation

Using a 3D intersecting pipe domain the authors performed a test study to validate the $\kappa - \epsilon$ model (Chapter 3) that was used to compute turbulent flow in a channel. The domain was similar to the test section used in the experimental work by Yalniz and Ozkan (2001) and also closely matching with Yuan et al. (1997). Water was used as the fluid with density of 1000 kg/m^3 and viscosity $0.001 \text{ Pa} - \text{s}$ at STP. Velocity boundary conditions were specified at inlets of the main and injection pipe, while the outlet was modeled as a convective (outflow) boundary. A combination of unstructured mesh near the junction and structured mesh away from it was used. The total mesh count was about 458,000 for the 3D domain. The entry length was chosen using the method described in the preceding section.

Comparison was made between the friction factor obtained from CFD results and that from the experiments of Yuan et al. (1997) and presented in Fig. A.2. The friction factor is defined as $f_t = \frac{\Delta p / \Delta x}{\rho \bar{u}_2^2 / 2D}$. The ratio of injection to the axial pipe flow rate for this study was $q_{in}/Q_1 = 0.1$. The Reynolds number is defined as $Re = \rho \bar{u}_2 D / \mu$, based on average outlet velocity. There is a slight deviation from

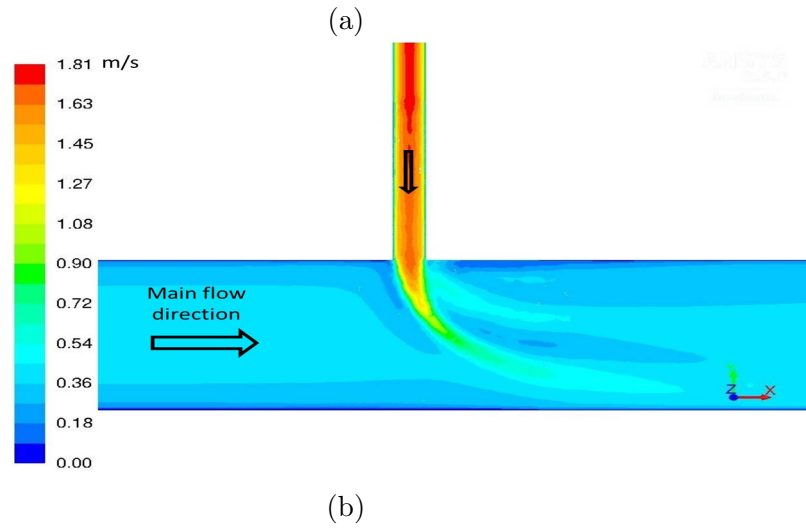
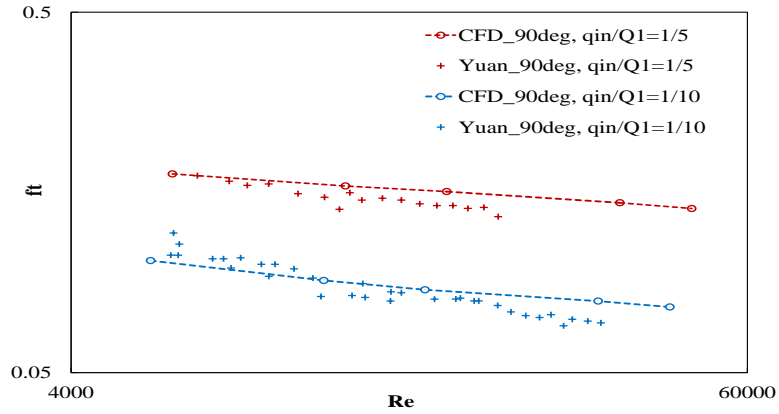


Figure A.2: (a) Friction factor comparison between $k-\epsilon$ model and experimental data from Yuan et al. (1997);(b) Contours of velocity magnitude near pipe junction at the center $z=0$ plane, $Re_{cf} = 9190$

the experimental results at lower Re , but fair agreement is obtained at higher Re . The above figure presents details of flow near the junction obtained from CFD. It shows the velocity magnitude contours near the junction. The dynamics of this flow interaction is being studied in greater detail, as this mixing process greatly affects the pressure drop, and hence the friction factor, across the junction.

D. User Defined Function for pressure boundary condition

```
/* UDF for hydrostatic head at pressure-inlet BC */
/* Pressure to be prescribed in Pascals*/

#include "udf.h"

/* Defining constants */
# define RHO 850.0
# define G 10.0
# define P_INIT 500
# define VOL_FAC 5.0
# define EQTIME 1.0

/* Change Zone IDs for each inlet, available from Fluent */
# define ZONEID_1 44
# define SIZERATIO 1

DEFINE_PROFILE(fill11,thread,index)
{
    Thread *t1;
    face_t f;
    real last_vol=0, new_vol=0, P=0;
    real height;
    real mass_flow1=0.0;
    Domain *domain;
    real time = CURRENT_TIMESTEP;
    int time_step = N_TIME;
    real current_time = CURRENT_TIME;
    real LB = VOL_FAC;
```

```

    t1 = Lookup_Thread(domain,ZONEID_1);    /*inlet*/
if(current_time<= EQTIME){
begin_f_loop(f,t1)
{
F_PROFILE(f,t1,index) = P_INIT; /* initial pressure */
F_UDMI(f,t1,0) = LB * P_INIT/(RHO*G); /* initial volume */
}end_f_loop(f,t1)
}
else{
begin_f_loop(f,t1){
mass_flow1 += F_FLUX(f,t1);
}end_f_loop(f,t1)

/*printf("Mass flow rate from the nozzle = %f\n", mass_flow1);*/
begin_f_loop(f,t1){last_vol = F_UDMI(f,t1,0);}end_f_loop(f,t1)
new_vol = last_vol + (mass_flow1 * time / RHO);
/*as mass flux is negative at inlet */
height = new_vol/(LB);
P = RHO * G * height; /*initial volume */

begin_f_loop(f,t1){
F_PROFILE(f,t1,index) = P;
F_UDMI(f,t1,0) = new_vol; /*assign new volume to memory */
}end_f_loop(f,t1)
}}

```